A&A, 683, A238 (2024)
https://doi.org/10.1051/0004-6361/202347099

Astronomy & Astrophysics

JADES: The emergence and evolution of Lyα emission and constraints on the intergalactic medium neutral fraction*

Gareth C. Jones[1], Andrew J. Bunker[1], Aayush Saxena[1,2], Joris Witstok[3,4], Daniel P. Stark[5], Santiago Arribas[6], William M. Baker[3,4], Rachana Bhatawdekar[7,8], Rebecca Bowler[9], Kristan Boyett[10,11], Alex J. Cameron[1], Stefano Carniani[12], Stephane Charlot[13], Jacopo Chevallard[1], Mirko Curti[14,3,4], Emma Curtis-Lake[15], Daniel J. Eisenstein[16], Kevin Hainline[5], Ryan Hausen[17], Zhiyuan Ji[5], Benjamin D. Johnson[16], Nimisha Kumari[18], Tobias J. Looser[3,4], Roberto Maiolino[3,4,2], Michael V. Maseda[19], Eleonora Parlanti[12], Hans-Walter Rix[20], Brant E. Robertson[21], Lester Sandles[3,4], Jan Scholtz[3,4], Renske Smit[22], Sandro Tacchella[3,4], Hannah Übler[3,4], Christina C. Williams[23], and Chris Willott[24]

(Affiliations can be found after the references)

Received 5 June 2023 / Accepted 20 December 2023

ABSTRACT

The rest-frame UV recombination emission line Lyα can be powered by ionising photons from young massive stars in star-forming galaxies, but the fact that it can be resonantly scattered by neutral gas complicates its interpretation. For reionisation-era galaxies, a neutral intergalactic medium will scatter Lyα from the line of sight, making Lyα a useful probe of the neutral fraction evolution. Here, we explore Lyα in JWST/NIRSpec spectra from the ongoing JADES programme, which targets hundreds of galaxies in the well-studied GOODS-S and GOODS-N fields. These sources are UV-faint ($-20.4 < M_{\rm UV} < -16.4$) and thus represent a poorly explored class of galaxy. We fitted the low spectral resolution spectra ($R \sim 100$) of a subset of 84 galaxies in GOODS-S with $z_{\rm spec} > 5.6$ (as derived with optical lines) with line and continuum models to search for significant line emission. Through exploration of the R100 data, we find evidence for Lyα in 17 sources. This sample allowed us to place observational constraints on the fraction of galaxies with Lyα emission in the redshift range $5.6 < z < 7.5$, with a decrease from $z = 6$ to $z = 7$. We also find a positive correlation between the Lyα equivalent width and $M_{\rm UV}$, as seen in other samples. We used these results to estimate the neutral gas fraction at $z \sim 7$, and our estimates are in agreement with previous results ($X_{\rm HI} \sim 0.5$–0.9).

Key words. galaxies: high-redshift – intergalactic medium – dark ages, reionization, first stars

1. Introduction

By studying the properties of galaxies at high redshifts (such as morphology, spectral energy distributions, and kinematics), we are able to chart how populations of galaxies have evolved through cosmic time. In individual galaxies we can study the buildup of gaseous reservoirs, the conversion of this fuel into stars, and the effects of feedback. By studying the overall galaxy population as a function of redshift, we can determine the evolution of the luminosity function, the star formation rate density, and the growth of supermassive black holes. In parallel, these studies shine light on the last great phase transition of the Universe, when the intergalactic medium (IGM) became ionised: the epoch of reionisation (EoR).

This epoch began at the end of the "cosmic dark ages", when the first stars formed (e.g. Villanueva-Domingo et al. 2018). The UV radiation of these objects created ionised regions (i.e. "bubbles"), which grew and merged together (e.g. Gnedin 2000). Observations suggest that the IGM was mostly ionised at $z \sim 6$ ($t_{\rm H} \sim 0.91$ Gyr; e.g. Fan et al. 2006), although the details of reionisation are still being derived (e.g. the drivers; Hutchison et al. 2019; Naidu et al. 2020; Endsley et al. 2021, topology; Pentericci et al. 2014; Larson et al. 2022; Yoshioka et al. 2022, and timeline; Christenson et al. 2021; Cain et al. 2021; Zhu et al. 2022). One of the most useful tools for studying this epoch is the bright Lyman-α line of hydrogen ($\lambda = 1215.67$ Å; hereafter Lyα).

As the lowest-energy transition ($n = 2 \rightarrow 1$) of the most abundant element, Lyα emission should be ubiquitous. But this radiation can be absorbed and re-radiated by any other hydrogen atom in the ground state (i.e. HI). For galaxies at $z \lesssim 6$, this repeated absorption and re-radiation by neutral gas inside a galaxy (i.e. resonant scattering) means that Lyα can be greatly reduced in intensity but also observed along sight lines far from the original emission region, as seen in large Lyα halos of ~10 kpc (e.g. Drake et al. 2022; Kikuta et al. 2023) or ~100 kpc (e.g. Steidel et al. 2000; Reuland et al. 2003; Dey et al. 2005; Cai et al. 2017; Li et al. 2021; Guo et al. 2023; Zhang et al. 2024).

For galaxies in the EoR, neutral gas in the IGM surrounding a galaxy can also scatter Lyα emission, resulting in a lower observed brightness (e.g. Fontana et al. 2010; Stark et al. 2010). In order for this emission to be observable, it must lie in an ionised bubble (e.g. Mason & Gronke 2020) and/or feature a significant outflow (e.g. Dijkstra & Wyithe 2010). So by comparing the fraction of galaxies with Lyα emission to the expected number from models (Lyα fraction; $X_{\rm Ly\alpha}$), we are able to place constraints on the HI filling fraction ($X_{\rm HI}$; e.g. Ono et al. 2012; Mason et al. 2018; Matthee et al. 2022).

Constraints on $X_{\rm Ly\alpha}$ have been placed for galaxies from $4 \lesssim z \lesssim 8$ (e.g. Stark et al. 2011, 2017; Curtis-Lake et al. 2012; Caruana et al. 2012, 2014; Ono et al. 2012; Schenker et al. 2014; Pentericci et al. 2018; Yoshioka et al. 2022) and down to

* Comparison sample is available at the CDS via anonymous ftp to cdsarc.cds.unistra.fr (130.79.128.5) or via https://cdsarc.cds.unistra.fr/viz-bin/cat/J/A+A/683/A238

$z \sim 2$ (e.g. Cassata et al. 2015). By comparing the observed evolution of $X_{\mathrm{Ly}\alpha}$ to that expected from different Lyα luminosity functions, some works have placed constraints on X_{HI}, suggesting that it quickly decreased from $\gtrsim$0.9 to ∼0 between $z \sim 8$ and $z \sim 6$ (e.g. Mason et al. 2018, 2019; Morales et al. 2021). Therefore, the study of galaxies in this short time interval (∼0.3 Gyr) is key to characterising the timeline of reionisation. While a number of studies have been undertaken, observations have been hampered by small sample sizes, limited volumes (prone to cosmic variance), or a focus on bright ($M_{\mathrm{UV}} \lesssim -20$) or strongly lensed sources (e.g. Hoag et al. 2019; Fuller et al. 2020; Bolan et al. 2022). Already, the *James Webb* Space Telescope (JWST) Near-Infrared Spectrograph (NIRSpec; Jakobsen et al. 2022; Böker et al. 2023) has seen great success in detecting Lyα (e.g. Bunker et al. 2023b; Jung et al. 2023; Roy et al. 2023; Tang et al. 2023). But to reduce sample variance and allow stronger conclusions, a wide-area survey down to $M_{\mathrm{UV}} \sim -18.75$ is needed (e.g. Taylor & Lidz 2014). With JWST, such a survey is possible.

The JWST Advance Deep Extragalactic Survey (JADES; Bunker et al. 2020; Eisenstein et al. 2023) is a cycle 1−2 guaranteed time observation (GTO) programme for observing the Great Observatories Origins Deep Survey (GOODS; Dickinson et al. 2003) north (N) and south (S) fields. It uses JWST/NIRSpec in multi-object spectroscopy mode (Ferruit et al. 2022) in both low spectral resolution (R100) and medium spectral resolution (R1000), in combination with the JWST/Near-Infrared Camera (NIRCam; Rieke et al. 2023).

This rich dataset is the subject of numerous ongoing investigations, including detailed modelling of the Lyα profiles using the R1000 spectra (e.g. asymmetry and velocity offsets; Saxena et al. 2024), analysis of the damping wings (Jakobsen et al., in prep.), and a search for Lyα overdensities that hint at large ionised bubbles (Witstok et al. 2024). In this work, we search for Lyα emission in the R100 spectra of data from GOODS-S for the purpose of placing constraints on the neutral gas fraction at $z \sim 6-8$. These fits are used to examine correlations between the Lyα rest-frame equivalent width ($\mathrm{REW}_{\mathrm{Ly}\alpha}$), redshift, and UV absolute magnitude.

We describe our sample in Sect. 2. The details and results of our R100 spectral fitting procedure are given in Sect. 3. These findings are discussed in Sect. 4, and we conclude in Sect. 5. We assume a standard concordance cosmology throughout: $(\Omega_\Lambda, \Omega_{\mathrm{m}}, h) = (0.7, 0.3, 0.7)$.

2. Sample

2.1. Observation overview

JADES consists of two survey depths: "Deep" and "Medium". The former allows for the characterisation of a small number of dimmer galaxies or more detailed study of individual sources at higher S/N, while the latter enables a statistical characterisation of the galaxy population at high-z. In addition, each tier has two stages with different selections: one based on existing *Hubble* Space Telescope (HST) imaging (followed by "/HST") and the other based on JWST/NIRCam imaging (followed by "/JWST"; see Eisenstein et al. 2023 for more details).

From the JADES survey, we utilised data from galaxies in GOODS-S in the Deep/HST (PID: 1210, PI: N. Lützgendorf), Medium/HST (PID: 1180, PI: D. Eisenstein), and Medium/JWST (PID: 1286, PI: N. Lützgendorf) sub-surveys. Target catalogues were created for each tier, with galaxies assigned priority classes based on photometric redshift, apparent UV-brightness, and visual inspection of existing ancillary data (for more details on Deep/HST priority classes, see Bunker et al. 2023a). Galaxies with $z_{\mathrm{phot}} > 5.6$ were collected from studies that selected sources based on the Lyman-break drop out selection (e.g. Bunker et al. 2004; Bouwens et al. 2015; Harikane et al. 2016), or Lyman-break galaxies (LBGs). This system ensures that both rare (e.g. bright, high-redshift, hosts of active galactic nuclei) and representative systems would be observed. Due to the geometrical constraints dictated by mask construction, galaxies were randomly selected for observation from each priority class.

Details of the data acquisition and reduction details are given in other works (Curtis-Lake et al. 2023; Carniani et al. 2024), which we summarise here. Targets were observed with three shutters in a three-point nod. In order to improve data quality, sub-pointings were created for each primary pointing by shifting the JWST/NIRSpec Multi-Shutter Array (MSA) by a few shutters in each direction. Due to failed shutters, not all targets were observable in all three sub-pointings. This results in exposure times of sources in R100 for Deep/HST of 33.6−100.8 ks for 253 observed sources. Medium/JWST features a similar setup, but with a lower R100 exposure time per target: 5.3−8.0 ks for 169 observed sources. While 1354 galaxies were observed in Medium/HST, the majority of the executions (8/12) were negatively affected by a short circuit in the MSA, making the data unusable. The mean exposure time for R100 per object of the usable data is 3.8 ks (Eisenstein et al. 2023). Observations were repeated for some of these objects with unusable data (364 sources), with a mean R100 exposure time per object of 7.5−11.3 ks.

The resulting raw data were calibrated using a pipeline developed by the European Space Agency (ESA) NIRSpec Science Operations Team (SOT) and the NIRSpec GTO Team, which includes corrections for outlier rejection (e.g. "snowballs"), background subtraction (using adjacent slits), wavelength grid resampling, and slit loss. This results in two-dimensional spectra with data quality flags, which were used to extract a one-dimensional spectrum and a noise spectrum.

2.2. Sample construction

The resulting spectra of all observed sources were visually inspected and strong emission lines (e.g. [OIII]λ5007, Hα) were fit. We imposed a lower redshift limit of $z_{\mathrm{spec}} > 5.6$ in order to ensure a sample of LBGs. This yielded a sample of 84 galaxies at $z \gtrsim 5.6$ (38 from Medium/HST, 13 from Medium/JWST, and 33 from Deep/HST) with precise spectroscopic redshifts (full details in Bunker et al. 2023a). Both R100 and R1000 spectra are available for these galaxies, and we used the R100 spectra in this work[1].

Our sample of 84 galaxies is composed of galaxies at $z_{\mathrm{spec}} > 5.6$ (i.e. LBGs) with cuts on UV brightness in HST broadband filters redwards of the Lyman break. Some sources were excluded from our sample for a lack of strong emission lines (i.e. a poorly constrained z_{spec}). While this results in a more complex sample than the uniform sample selection of some previous studies (e.g. Pentericci et al. 2018; Yoshioka et al. 2022), this inhomogeneity is taken into account through the error spectrum of each source and a completeness analysis.

[1] Details of the R1000 analysis are presented in an associated paper (Saxena et al. 2024).

3. Combined Lyα and continuum fit

At these high redshifts, the spectra exhibit a strong continuum break at the Lyα wavelength at the redshift of the galaxy. The deep sensitivity of the R100 data allows us to simultaneously characterise any Lyα emission and the underlying continuum of each source. To do this, we examined whether a two-component model (i.e. line and continuum) or a single-component model (i.e. only continuum) better fits the extracted spectrum of each source using LMFIT (Newville et al. 2014). This process is detailed below.

3.1. Resolution effects

Due to the low spectral resolution of the R100 data, we had to consider both the wavelength grid and spectral dispersion. The spectral pixels in our calibrated data are large ($\Delta v \sim 2000-2600\,\mathrm{km\,s^{-1}}$ per pixel at the redshifted Lyα wavelength for galaxies at $z \sim 5.6-10$). Furthermore, for galaxies observed in the EoR this wavelength is near the minimum of the PRISM resolving power curve[2], with $R \sim 30$. This implies that the line-spread function (LSF) has a full width at half maximum of $\sim 10^4\,\mathrm{km\,s^{-1}}$. Although for a compact source that does not fill the slit, the resolving power will in practice be higher by as much as a factor of 2 (de Graaff et al. 2024).

The low resolution also makes it impossible to characterise the Lyα profile (e.g. asymmetry, velocity offset). Instead, the Lyα emission can be approximated as additional flux in the first spectral bin redwards of the Lyα break, which is spread into neighbouring bins by the LSF.

To demonstrate how this affects the interpretation of R100 spectra, we first created a higher-resolution ($\Delta\lambda = 0.001\,\mu\mathrm{m}$, or $R \sim 730$) model of a Lyα break (modelled as a step function) at $z = 7$ with no Lyα flux (blue line in the top panel of Fig. 1). If we account for the LSF by convolving the spectrum with a Gaussian ($\sigma_R = \lambda_{\mathrm{Ly}\alpha}/R/2.355$), the break becomes an S-shaped curve instead (orange histogram). Rebinning this curve to the coarser R100 wavelength grid maintains the curve, but at lower resolution (green histogram).

If we add Lyα flux with a given $\mathrm{REW_{Ly\alpha}}$ to the intrinsic high-resolution model as additional flux in the first spectral bin redwards of the Lyα break, convolve the model with the LSF, and re-bin the result to the R100 spectral grid, we find the profiles shown in the lower panel of Fig. 1. The line flux is spread from one low-resolution pixel into a Gaussian that spans both sides of the Lyα break. Even high-$\mathrm{REW_{Ly\alpha}}$ lines (e.g. 100 Å) have low peaks (here 4× the continuum level). In addition, low-$\mathrm{REW_{Ly\alpha}}$ lines (<20 Å) feature very low amplitudes, and instead appear similar to a pure continuum model with a blueshifted Lyα break.

With this in mind, our model fitting procedure begins with a high-resolution spectral model, which is convolved with a Gaussian to account for the resolving power and then rebinned to the R100 spectral grid. This allows us to compare the observed and model spectra directly, in order to extract the intrinsic continuum and Lyα flux.

3.2. Model description

We first assumed that the underlying continuum can be approximated by a power law and used a Heaviside step function to represent the Lyα break (see Appendix B for a discussion of this assumption). This continuum-only model only features two variables: the continuum value at a rest-frame wavelength of 1500 Å ($S_{\mathrm{C,o}}$) and the spectral slope just redwards of Lyα (n; ~1300−1500 Å rest-frame), which is not fixed to the redder (i.e. ~1400−2300 Å rest-frame) spectral slope β derived by Saxena et al. (2024).

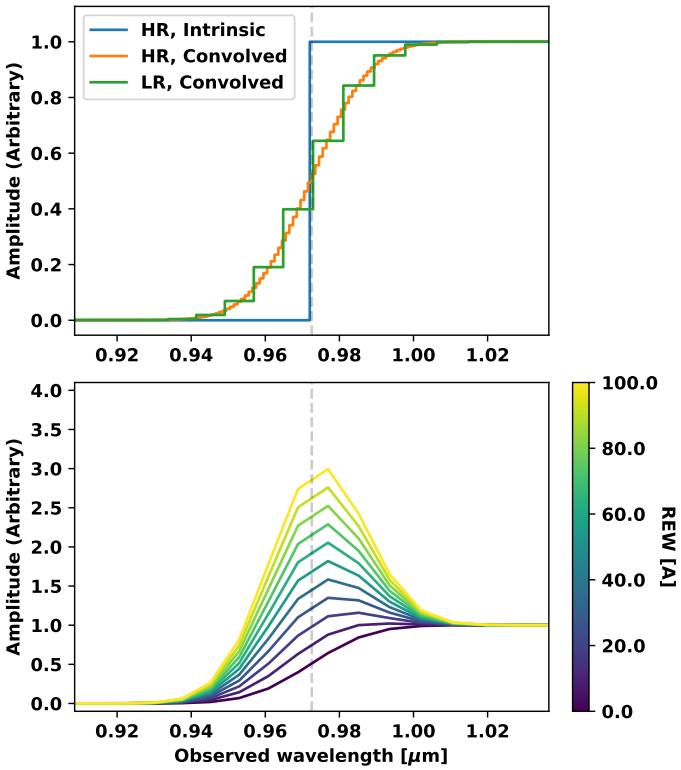

Fig. 1. Demonstration of how Lyα break and emission for a source at $z = 7$ are affected by the low resolving power of our observations. The top panel shows how a step function (blue line) is affected by the resolving power on a high-resolution ($\Delta\lambda = 0.001\,\mu\mathrm{m}$) spectral grid (orange curve), and how this curve would appear on the R100 spectral grid (green steps). If we add Lyα emission with a given $\mathrm{REW_{Ly\alpha}}$ in the first high-resolution spectral bin redwards of the break and then account for the LSF and R100 spectral bin, we find the curves in the lower panel.

In the case where both continuum and Lyα emission are detected, the line emission will have a REW of

$$\mathrm{REW_{Ly\alpha}} = \frac{F_{\mathrm{Ly}\alpha}}{(1+z)S_C(\lambda_{\mathrm{Ly}\alpha,\mathrm{obs}})}, \quad (1)$$

where $F_{\mathrm{Ly}\alpha}$ is the total line flux of Lyα. As discussed in Sect. 3.1, the low spectral resolution of the R100 data dictates that our line emission model is simple. Our combined line and continuum model thus has three variables: those of the continuum model (i.e. $S_{\mathrm{C,o}}$ and n) and $\mathrm{REW_{Ly\alpha}}$.

For both the continuum and line+continuum models, we first created a spectral grid of high resolution ($\Delta\lambda = 0.001\,\mu\mathrm{m}$) and populated each bin using a continuum-only or continuum and line model. As discussed in Sect. 3.1, we then convolved the spectrum with a Gaussian that accounts for the LSF. We first considered using a Gaussian based on the theoretical resolving power as recorded in the JWST documentation ($\sigma_{\mathrm{R}} = \lambda_{\mathrm{Ly}\alpha}/R/2.355$). However, this was calculated assuming a source that illuminates the slit uniformly, which is not the case for the relatively compact sources in our sample. Detailed LSFs for

[2] As recorded in the JWST documentation: https://jwst-docs.stsci.edu/jwst-near-infrared-spectrograph/nirspec-instrumentation/nirspec-dispersers-and-filters

the sources in Deep/HST have been calculated (de Graaff et al. 2024), which reveal that the actual LSF is smaller than the theoretical value, by a factor of up to ∼2.4. However these models are not available for our whole sample. To account for the LSF in a uniform manner, we convolved the model spectrum with a Gaussian of width $F_R\sigma_R$, where F_R is allowed to vary. These data were then re-binned to the R100 spectral grid of an observation.

3.3. Fitting procedure

We used LMFIT with a "leastsq" minimiser to fit each convolved model to a subset of the observed spectrum. Each data point was weighted by its associated inverse variance (as derived from the error spectrum).

We limited the fit subset to the wavelength range $\left[\left(\lambda_{Ly\alpha} \pm (0.03\,\mu m)\right) \times (1+z)\right]$, with a minimum of $\geq 0.75\,\mu m$. This range was chosen to avoid including excessive amounts of noisy data at blue wavelengths below the Lyα break, and to only fit the continuum just redwards of Lyα, avoiding nearby emission lines (e.g. [CIV]$\lambda\lambda$1548, 1551 and HeIIλ1640).

While precise systemic redshifts for each source have been derived using fits to strong lines (e.g. [OIII]λ5007 and Hα) using the higher spectral resolution gratings (Bunker et al. 2023a), it is possible that the Lyα emission is shifted into a neighbouring spectral bin by a large velocity offset (i.e. up to a few hundred km s^{-1}; Erb et al. 2014; Marchi et al. 2019) or a different binning scheme between the gratings and prism. This is accounted for by allowing the redshift of Lyα emission to vary from the systemic redshift within the R100 bin, taking the result with the lowest χ^2.

Next, we considered the lowest REW line that we can detect for each source. Because the line emission is spread from one into multiple channels by convolution with the LSF, we could approximate the 1σ limit on $\mathrm{REW}_{Ly\alpha}$ in the R100 spectrum as

$$\Delta\mathrm{REW}_{Ly\alpha,1\sigma} = \frac{\sqrt{2\pi}E(\lambda_{Ly\alpha,obs})F_R\sigma_R}{(1+z)S_{C,Ly\alpha}}, \quad (2)$$

where $F_R\sigma_R$ is the width of the LSF and $E(\lambda)$ is the error spectrum.

The results of the continuum ("C") and line and continuum ("L+C") are examined, and a definite Lyα detection is reported if both of the following criteria are met:

- The "L+C" fit features a lower χ^2_{red} than the "C" fit.
- The best-fit $\mathrm{REW}_{Ly\alpha}$ is greater than $2.5\Delta\mathrm{REW}_{Ly\alpha,1\sigma}$.

When Lyα is detected, we take the best-fit $\mathrm{REW}_{Ly\alpha}$ value and its associated uncertainty from our fit. Otherwise, we treat the Lyα line as undetected, and use $3\Delta\mathrm{REW}_{Ly\alpha,1\sigma}$ as an upper limit.

3.4. Results

With this definition, we find that 17 galaxies in our sample feature significant Lyα emission from the R100 spectra alone. The best-fit models of these detections are shown in Figs. 2 and A.1 while the best-fit parameters of all galaxies in our sample are presented in Appendix C.

For comparison, we present $\mathrm{REW}_{Ly\alpha}$ values derived by taking the continuum values from this work and the Lyα fluxes measured from the R1000 spectra by Saxena et al. (2024). These line fluxes were only measured for galaxies at $z > 5.8$ in the Deep/HST and Medium/HST tiers in GOODS-S (excluding Medium/JWST, where there are no $z > 5.8$ galaxies detected in Lyα emission). For some of these sources, Lyα fell into the unobservable chip gap, so no Lyα is given.

We note that the use of the low spectral resolution PRISM/CLEAR grating/filter combination ($R \sim 100$) results in detections or limits that are in agreement (i.e. within 3σ) with the higher-resolution R1000 data for every source. This is encouraging, as the latter is more sensitive to low equivalent width lines. For example, Bunker et al. (2023b) find that Lyα is not observable in the R100 spectrum of GNz-11, but is clearly detected in the R1000 spectrum. This can also be seen in our sources that are undetected in the prism, but have a 3σ $\mathrm{REW}_{Ly\alpha,R100}$ upper limit that agrees with a smaller $\mathrm{REW}_{Ly\alpha,R1000}$ value (i.e. our $\mathrm{REW}_{Ly\alpha}$ upper limit from the prism is consistent with the value of the $\mathrm{REW}_{Ly\alpha}$ inferred from the grating detection).

From our R100 fitting analysis, we find that 17 of the 84 galaxies in our sample are detected in Lyα. In the following subsections, we analyse the properties of these detections.

3.5. Completeness analysis

As seen in Eq. (2), our REW sensitivity is dependent on observational parameters (error spectrum and LSF) as well as source properties (redshift and continuum flux). To further complicate matters, the error spectrum features higher values at small wavelengths, resulting in larger uncertainties in $E(\lambda_{Ly\alpha,obs})$ for lower redshift sources. Our sample is quite diverse in redshift, continuum strength (i.e. M_{UV}), and sensitivity (i.e. Deep and Medium tiers). So while Eq. (2) can be used as a limit on REW, it does not capture the breadth of galaxy properties in our sample, and an estimation of the completeness of our sample is required (e.g. Thai et al. 2023).

To begin, we assumed a similar model to the previous subsections: a power-law continuum, a Lyα break given by a Heaviside step function, and Lyα emission quantified as an REW. The mean uncertainty spectra for each tier were calculated by averaging the corresponding error spectra. For each galaxy, we took the best-fit continuum strength (M_{UV}) and redshift (z), and created 50 mock spectra by sampling from uniform distributions of $\beta = [-2.5, 2.5]$, and $F_R = [0.1, 0.8]$. This process was repeated for three REW values (25 Å, 50 Å, and 75 Å). Gaussian noise was added based on the error spectrum. Each of these 12 900 model spectra was fit with the procedure outlined in Sect. 3.3, and the completeness for each galaxy and REW value was then estimated as the fraction of models that are well fit (i.e. that return a REW value within 3σ of the input value).

This analysis yields an average completeness for our sample of $C_{25\,Å} = 0.33$, $C_{50\,Å} = 0.60$, and $C_{75\,Å} = 0.74$. As expected, the completeness of each tier increases with REW. Our completeness at REW = 25 Å is low, which results in poor constraints on $X_{Ly\alpha}$ and X_{HI} (see Sects. 4.3 and 4.4). We use these completeness values to derive corrected Lyα fractions in the next section.

4. Discussion

4.1. Source properties

To demonstrate the multi-tier complexity of our sample, we show the systemic redshift (based on the identification of rest-frame optical lines; Bunker et al. 2023a) and the 1500 Å continuum magnitude (hereafter M_{UV}), separated by survey tier (Fig. 3). Previous studies defined UV-faint galaxies as those with $M_{UV} > -20.25$ (e.g. Curtis-Lake et al. 2012), which shows that most of the JADES sample contains faint sources. The high-redshift bins ($z > 8$) are dominated by the Deep/HST sources, but the $5.6 < z < 7.5$ regime is well explored by all three

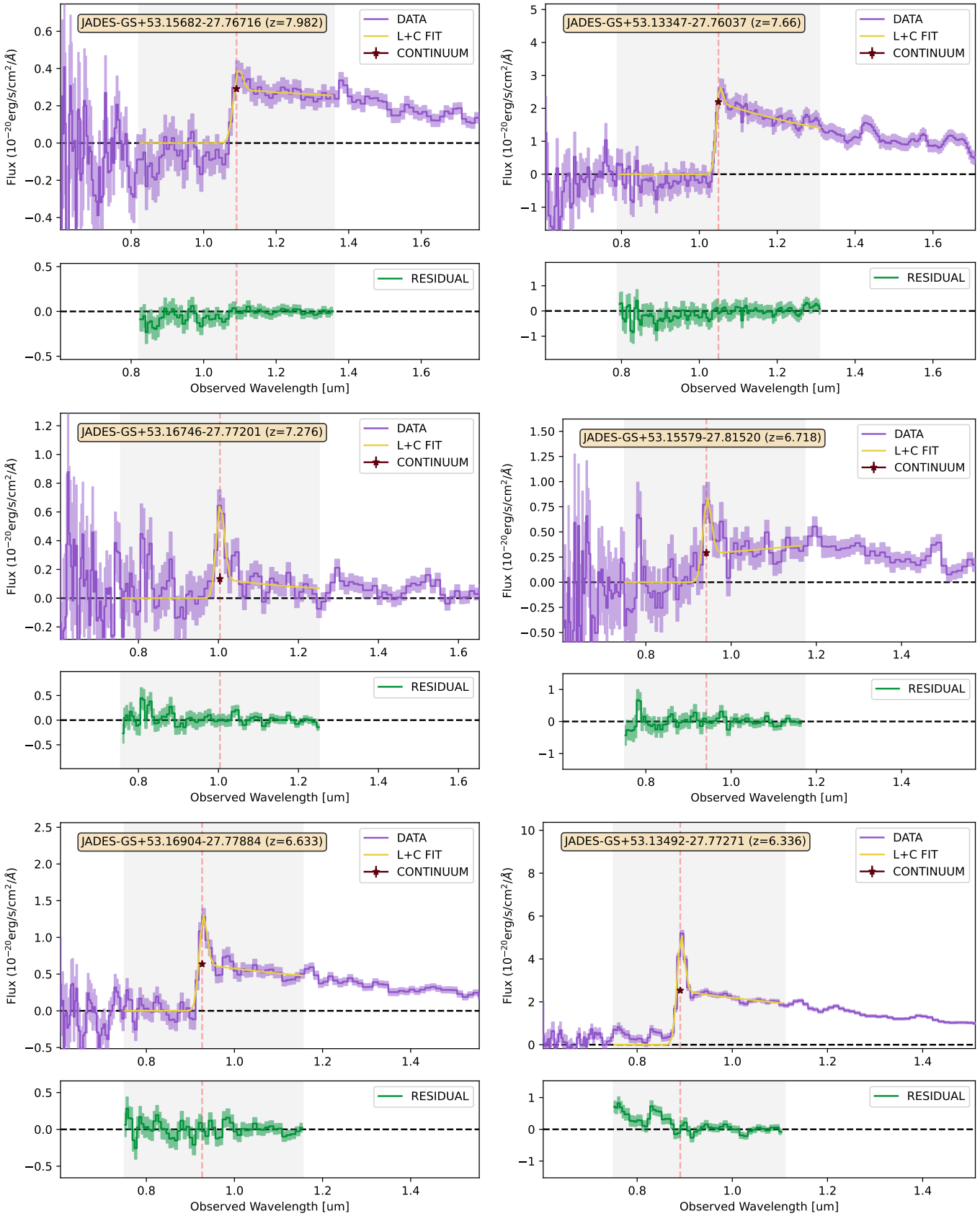

Fig. 2. Results of fitting a line plus continuum model to observed JADES R100 data, for sources detected in Lyα emission (denoted by "L+C FIT"). In each top panel, we show the observed spectrum (purple line) with an associated 1σ error (shaded region). The best-fit model, which includes the effects of the LSF, is shown by a yellow line. Fitting was performed using the wavelength range that is shaded grey. The continuum value at the redshifted Lyα wavelength is represented by a brown star. The bottom panel shows the residual. Continued in Fig. A.1.

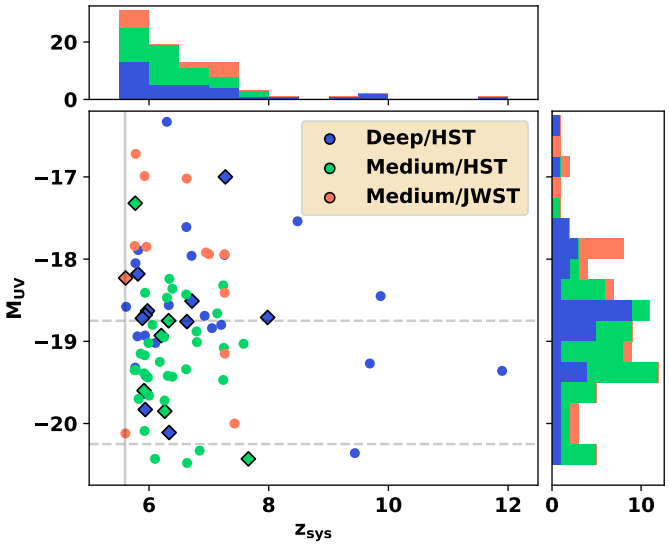

Fig. 3. M_{UV} (from NIRSpec spectra; see Appendix D) versus systemic redshift (based on optical lines) for our sample. Galaxies observed in different tiers are coloured differently. Sources detected in Lyα emission are shown as diamonds with black outlines. Horizontal dashed lines show M_{UV} values of −18.75 and −20.25, while the vertical grey line shows our lower redshift cutoff ($z_{sys} > 5.6$).

subsamples. The overall sample is well sampled in the $M_{UV} \sim -19.5$ to -17.5 regime, but extends down to $M_{UV} \sim -16.5$.

The sources with Lyα detections in R100 data are contained within $z \sim 5.6 - 8.0$, and span a wide range of $M_{UV} \sim -20.5$ to -17 . Of the 51 sources in the Medium tiers, 7 are detected in Lyα ($\sim 14\%$). On the other hand, 10 of the 33 Deep galaxies are Lyα-detected ($\sim 30\%$). In the next subsection, we explore the limits that the non-detections imply.

4.2. Equivalent width–UV magnitude relation

A recent analysis of JWST/NIRSpec MSA data from the Cosmic Evolution Early Release Science (CEERS) survey (Tang et al. 2023) and data at lower redshift showed a positive correlation between $REW_{Ly\alpha}$ and M_{UV} for a sample of galaxies with high O32 values (i.e. a high level of ionisation). To investigate this relation further, we first collected a literature sample of galaxies with reported spatial positions, spectroscopic redshifts, $REW_{Ly\alpha}$ from spectral observations, and M_{UV} values (including that of Tang et al. 2023; see Appendix E) and split this sample into different redshift bins (Fig. 4).

In each redshift bin, there appears to be a positive correlation between $REW_{Ly\alpha}$ and M_{UV}, such that UV-fainter (higher M_{UV}) objects feature higher Lyα equivalent widths. To illustrate this, we fitted a simple model to the data, which resulted in positive slopes (see the dashed black line). We do not present the fit values or uncertainty, as the literature sample is not constructed with a single set of criteria.

While this trend may be physical, it may also be influenced by the sensitivity limits of observations. As a test of this, we created a set of simulated R100 spectra that do not feature any relation between REW and M_{UV}, fitted them with our method, and plotted the resulting best-fit values and upper limits (see Appendix F). This test shows that we are not able to recover UV-faint, low-REW galaxies, resulting in an apparent positive correlation. While this does not affect the conclusion of other works, we cannot claim a correlation based on our data.

4.3. Lyα fraction

Next, we derived the fraction of galaxies in our sample that are detected in Lyα emission ($X_{Ly\alpha}$). This has been a focus of multiple studies over the past decade (e.g. Stark et al. 2011, 2017; Curtis-Lake et al. 2012; Ono et al. 2012; Caruana et al. 2012, 2014; Schenker et al. 2014; Pentericci et al. 2018; Yoshioka et al. 2022), where subsamples are usually created according to cuts on M_{UV} and the value of $REW_{Ly\alpha}$.

The most well-studied sample for $X_{Ly\alpha}$ evolution is that of galaxies with $-21.75 < M_{UV} < -20.25$ and $REW_{Ly\alpha} > 25$ Å (e.g. Fontana et al. 2010; Stark et al. 2011, 2017; Ono et al. 2012; Curtis-Lake et al. 2012; Schenker et al. 2012, 2014; Pentericci et al. 2014, 2018; Cassata et al. 2015; Yoshioka et al. 2022). For these galaxies, studies have hinted at a steep increase in $X_{Ly\alpha}$ between $z = 7$ and 6, with a shallower drop off between $z = 6$–4. Since the JADES sample contains fainter galaxies (see Fig. 3), we were instead able to focus on fainter galaxies ($M_{UV} > -20.25$).

We first divided our sample of galaxies into discrete redshift bins and calculated effective sample sizes by summing their completeness values (Sect. 3.5). The Lyα fraction was then found by dividing the number of galaxies in the redshift bin that meet the REW limit by the effective sample size (e.g. Caruana et al. 2012). This was repeated for three cuts on $REW_{Ly\alpha}$ (>25 Å, >50 Å, or >75 Å), and we compared them to observed fractions from the literature for galaxies fainter than $M_{UV} > -20.25$ (Stark et al. 2010, 2011; Ono et al. 2012; Schenker et al. 2012, 2014; Pentericci et al. 2014, 2018; see Fig. 5).

For galaxies with $-20.25 < M_{UV} < -18.75$, previous studies have shown that the fraction for EW > 25 Å increases from $z = 7$ to $z = 6$ with evidence for a decrease to $z = 4$, presumably due to the onset of IGM neutrality. Due to the low completeness of our sample at 25 Å (see Sect. 3.5), we are not able to place tight constraints on $X_{Ly\alpha}$ in this REW regime. Despite this, our estimates are in agreement with previous findings. The higher completeness at REW > 50 Å and REW > 75 Å results in agreement with previous results.

Overall, our sample supports a rise in the Lyα fraction between $z = 7$ and $z = 6$, as seen in previous studies. Since JADES is ongoing, future investigations will include more data and yield tighter constraints on the evolution of this quantity. Even with our current data, we are able to constrain the IGM neutral fraction, as seen in the next subsection.

4.4. Constraints on the neutral fraction

The observed Lyα fraction of galaxies for a given redshift, M_{UV} bin, and $REW_{Ly\alpha}$ limit provides valuable information on the neutral fraction of the IGM (X_{HI}). This is due to the fact that the evolution of $X_{Ly\alpha}(z \lesssim 6)$ is dependent only on galaxy properties, while at $z \gtrsim 6$ it is also dependent on the properties of IGM transmission. Some studies compared observed $X_{Ly\alpha}(z \sim 7)$ with the fraction expected from simulations, resulting in a range of estimates for $X_{HI}(z = 7)$: $\lesssim$0.3 (Stark et al. 2010), ∼0.5 (Caruana et al. 2014), $\gtrsim$0.51 (Pentericci et al. 2014), ∼0.6–0.9 (Ono et al. 2012), $\lesssim$0.7 (Furusawa et al. 2016). This discrepancy may be partially explained by sample properties (e.g. difference in M_{UV} ranges and small sample sizes).

The conversion from $X_{Ly\alpha}$ to X_{HI} is non-trivial, and is dependent on the simulation used for comparison to observations. For example, the semi-numerical code DexM (Mesinger & Furlanetto 2007; Mesinger et al. 2011; Zahn et al. 2011) has been used by some works (e.g. Dijkstra et al. 2011;

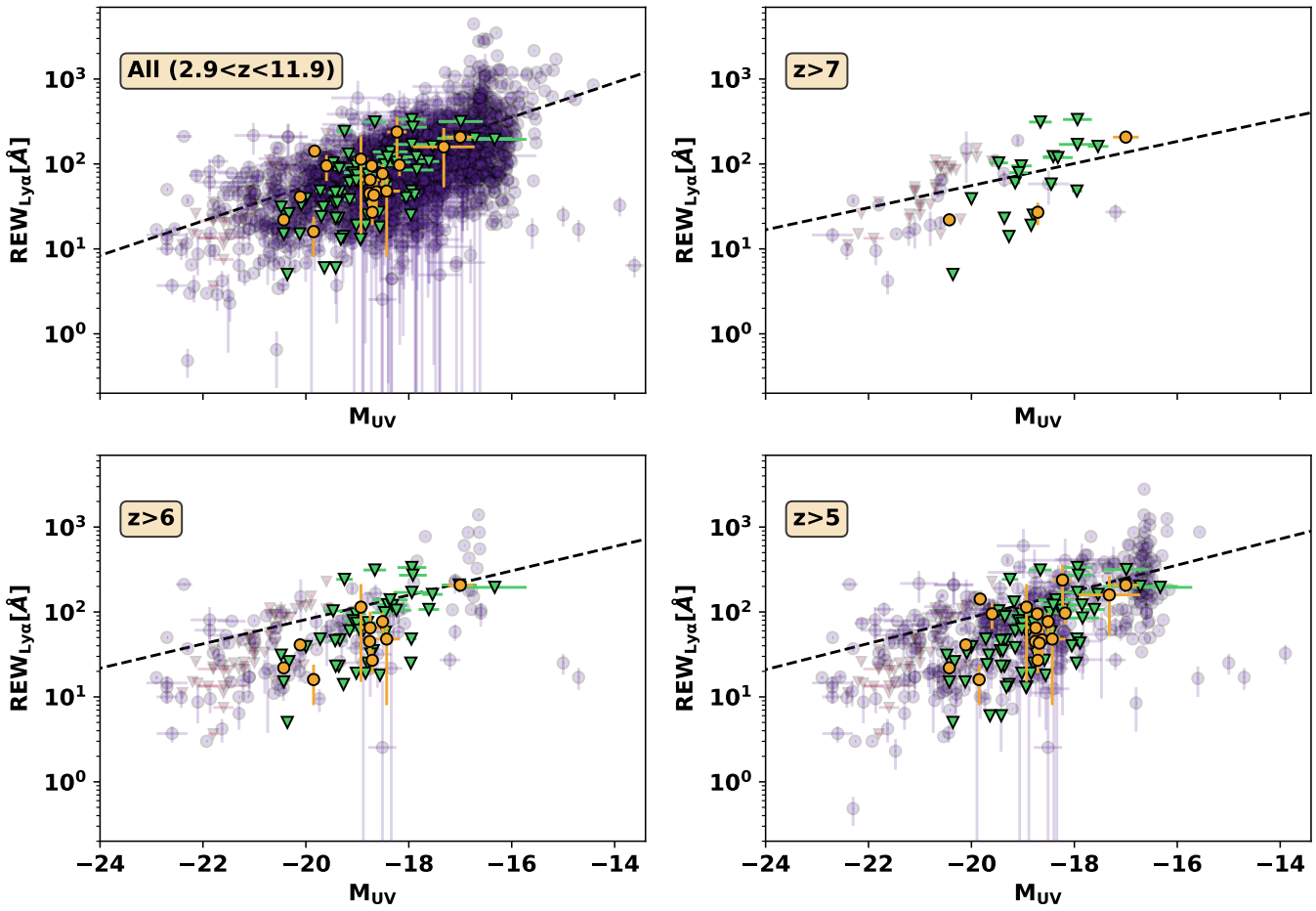

Fig. 4. Distribution of Lyα REWs as a function of $M_{\rm UV}$ for our sample (orange circles for detections and green triangles for 3σ upper limits) and from the literature (purple circles for detections and red triangles for 3σ upper limits). An illustrative fit to the detections is shown by the black dashed line. See Appendix E for details of the literature sample.

Pentericci et al. 2014) to create three-dimensional models of galaxy halos, determine how they ionise their surroundings, and characterise their redshift evolution. The outputs of this process (e.g. $X_{\rm Ly\alpha}$) can then be compared to observations.

While an updated simulation is beyond the scope of this work, we can use our $X_{\rm Ly\alpha}$(REW$_{\rm Ly\alpha}$) values at $z \sim 7$ to generate a cumulative distribution function (CDF) of REW$_{\rm Ly\alpha}$, and compare this to model outputs of Pentericci et al. (2014). This model is appropriate for galaxies with $-20.25 < M_{\rm UV} < -18.75$ and assumes $N_{\rm HI} = 10^{20}$ cm^{-2} and a wind speed of 200 km s^{-1}, but with a variable neutral fraction. It is based on the assumption that the Lyα CDF at $z = 6$ and $z = 7$ are intrinsically the same, but are observed to differ because of neutral IGM attenuation at $z = 7$. As seen in Fig. 6, higher values of $X_{\rm HI}$ result in less Lyα transmission, and thus a steeper CDF. Literature values (Ono et al. 2012; Schenker et al. 2012; Pentericci et al. 2014, 2018) appear to argue for a value of $X_{\rm HI} \sim 0.5$–0.9.

Our results (using a wide redshift bin of $6 < z < 8$) are in agreement with those of the previous studies (e.g. Mason et al. 2018), suggesting an approximate $X_{\rm HI}$ of ~0.2–0.7. We note that our P(REW > 25 Å) point is influenced by poor completeness, and thus does not provide a constraint. We note that this $M_{\rm UV}$ range is not optimised for our sample, and a future work will investigate how the redshift evolution ($z = 8$–6) of P(>REW) for $-20.4 < M_{\rm UV} < -16$ galaxies can be used to constrain $X_{\rm HI}(z)$.

The $X_{\rm HI}$ range of our analysis agrees with previous analyses that use the REW$_{\rm Ly\alpha}$ cumulative distribution (e.g. Schenker et al. 2014; Pentericci et al. 2014, 2018) as well as simulations (e.g. Mason et al. 2018). This suggests that our estimates of P(>REW) have not been underestimated due to the NIRSpec MSA shutters ($0.2'' \sim 1$ kpc at $z \sim 7$) missing Lyα flux from extended halos, as noted by Jung et al. (2023). In this previous study, $F_{\rm Ly\alpha,MSA}$ for one observed source was only 20% of the value derived using the Multi-Object Spectrometer for Infra-Red Exploration (MOSFIRE) instrument on the Keck I telescope. On the other hand, Tang et al. (2023) found agreement between MSA- and ground-based estimates of $F_{\rm Ly\alpha}$ for four $z \sim 7$–9 galaxies (but with large uncertainties for two sources). In addition, large Lyα halos are commonly seen at low-z, but will not have time to evolve for high-redshift sources. So while slit losses are unlikely to affect our results, this effect can be further investigated by observing representative sources with the NIRSpec Integral Field Unit (IFU; field of view of $3'' \times 3''$), or forward modelling the slit losses in simulations.

5. Conclusions

In this work we present the first constraints on Lyα emission using JWST/NIRSpec MSA R100 spectra from the JADES survey. The increased sensitivity of this instrument enables deeper investigations of faint galaxies in the early Universe. Our sample consists of 84 galaxies at $z > 5.6$, each with secure spectroscopic redshifts (Bunker et al. 2023a). While the sample is concentrated at $5.6 \lesssim z \lesssim 7.5$, we included sources up to

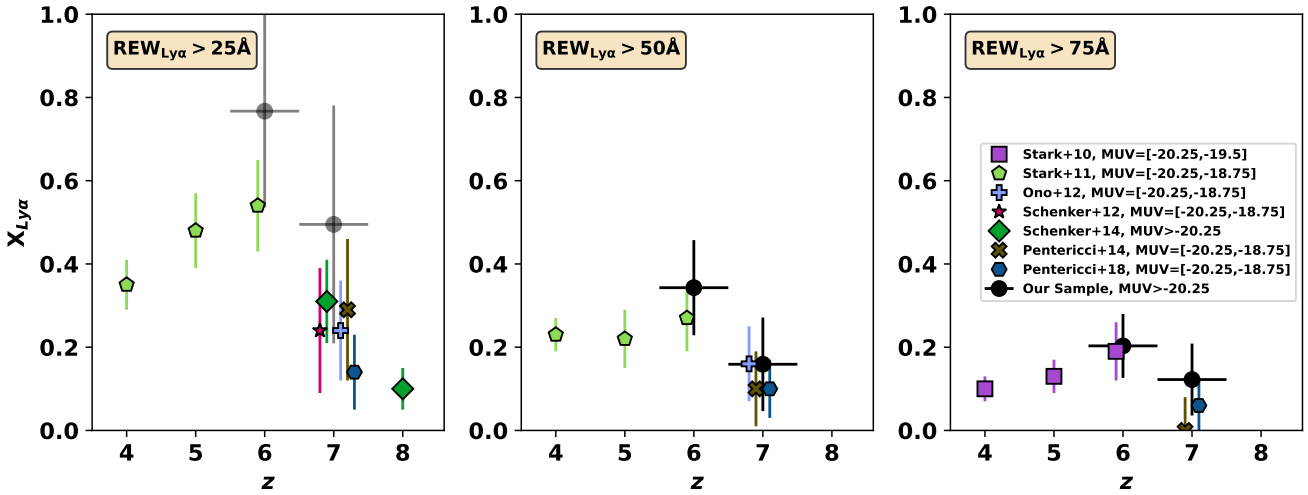

Fig. 5. Fraction of observed galaxies detected in Lyα emission with REW$_{Ly\alpha}$ > 25 Å (left), REW$_{Ly\alpha}$ > 50 Å (centre), and REW$_{Ly\alpha}$ > 75 Å (right). Derived fractions from the literature are shown by coloured markers. For the central panel, note that Stark et al. (2011) and Ono et al. (2012) used a REW limit of >55 Å. The fractions derived using only the observed JADES galaxies are shown by black points. Our REW > 25 Å values (grey) are likely affected by low completeness.

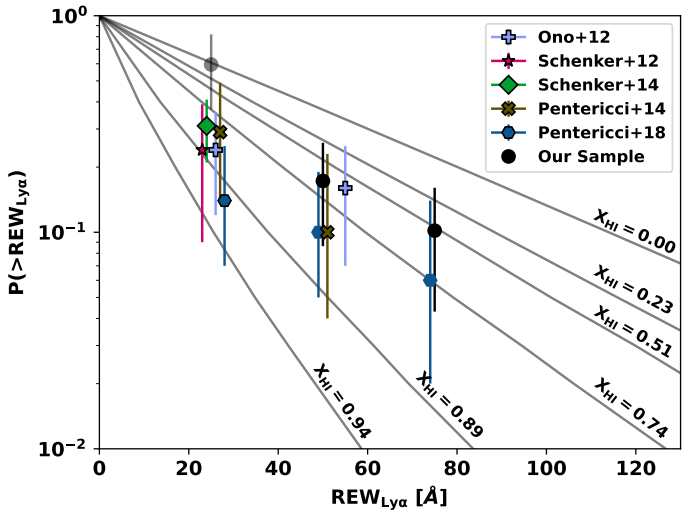

Fig. 6. Cumulative distribution for Lyα REW for UV-faint galaxies ($-20.25 < M_{UV} < -18.75$) at $z \sim 7$. Each solid line shows the expected distribution for a model with $N_{HI} = 10^{20}$ cm^{-2} and a wind speed of 200 km s^{-1}, but with a different neutral fraction (Pentericci et al. 2014). Estimates from the literature (Ono et al. 2012; Schenker et al. 2012, 2014; Pentericci et al. 2014, 2018) are shifted by 1 Å for visibility. Our P(REW > 25 Å) point (grey) is likely affected by low completeness.

$z \sim 12$. In addition, the $M_{UV} \sim -19.5$ to -17.5 range is well probed, but we included sources that are fainter ($M_{UV} \sim -16$) and brighter ($M_{UV} \sim -20.4$).

By fitting each spectrum with a line and/or continuum model, accounting for the spectral dispersion, and comparing the relative goodness-of-fit values, we find that 17 sources at $z \sim 5.6-8.0$ show evidence for Lyα emission in R100. The strong continuum of each source enabled us to estimate the continuum flux (and M_{UV}) at the Lyα wavelength directly from the spectra. We derived Lyα REWs for each source.

We built a large comparison sample from the literature of galaxies with estimates of spectroscopic redshifts, M_{UV}, and REW$_{Ly\alpha}$. By combining the JADES and literature samples, we find that the reported positive correlation between M_{UV} and REW$_{Ly\alpha}$ is supported for galaxies in multiple redshift bins, but the observed correlation in our data may be caused by sensitivity effects.

Next, we calculated the redshift evolution of the Lyα fraction ($X_{Ly\alpha}$) in bins of REW$_{Ly\alpha}$. Due to the faintness of the JADES sample ($M_{UV} \gtrsim -20.4$), we were able to place constraints on the poorly studied faint, high-redshift ($z \sim 6-7$) evolution of this fraction: a shallow increase from $z = 7$ to $z = 6$ for REW > 50 Å and REW > 75 Å.

The distribution of REW$_{Ly\alpha}$ values was then used to place a constraint on the neutral fraction (X_{HI}) at $z \sim 7$ using the Pentericci et al. (2014) model. Our results indicate $X_{HI} \sim 0.2-0.7$, which is in agreement with previous studies.

The JADES survey is still ongoing, so this dataset will expand with time. In addition, many sources feature higher-resolution R1000 spectra, which enable further science cases such as Lyα velocity offset and line asymmetry analysis, damping wing modelling, and environments of Lyα emitters (LAEs). Combined, these analyses will reveal the details of reionisation in unprecedented detail.

Acknowledgements. G.C.J., A.J.B., A.S., A.J.C., and J.C. acknowledge funding from the "FirstGalaxies" Advanced Grant from the European Research Council (ERC) under the European Union's Horizon 2020 research and innovation programme (Grant agreement No. 789056). J.W., R.M., W.M.B., T.J.L., L.S., and J.S. acknowledge support by the Science and Technology Facilities Council (STFC) and by the ERC through Advanced Grant 695671 "QUENCH". J.W. also acknowledges funding from the Fondation MERAC. R.M. also acknowledges funding from the UKRI Frontier Research grant RISEandFALL and from a research professorship from the Royal Society. S.A. acknowledges support from Grant PID2021-127718NB-I00 funded by the Spanish Ministry of Science and Innovation/State Agency of Research (MICIN/AEI/ 10.13039/501100011033). R.B. acknowledges support from an STFC Ernest Rutherford Fellowship (ST/T003596/1). This research is supported in part by the Australian Research Council Centre of Excellence for All Sky Astrophysics in 3 Dimensions (ASTRO 3D), through project number CE170100013. S.C. acknowledges support by European Union's HE ERC Starting Grant No. 101040227 – WINGS. E.C.L. acknowledges support of an STFC Webb Fellowship (ST/W001438/1). D.J.E., B.D.J., and B.E.R. acknowledge a JWST/NIRCam contract to the University of Arizona NAS5-02015. D.J.E. is supported as a Simons Investigator. Funding for this research was provided by the Johns Hopkins University, Institute for Data Intensive Engineering and Science (IDIES). R.S. acknowledges support from a STFC Ernest Rutherford Fellowship (ST/S004831/1). H.Ü. gratefully acknowledges support by the Isaac Newton Trust and by the Kavli Foundation through a Newton-Kavli Junior Fellowship. The research of CCW is supported

by NOIRLab, which is managed by the Association of Universities for Research in Astronomy (AURA) under a cooperative agreement with the National Science Foundation. G.C.J. would like to thank C. Witten and N. Laporte for valuable insight into the sample. We thank the anonymous referee for constructive feedback that has enhanced this work.

References

Böker, T., Beck, T. L., Birkmann, S. M., et al. 2023, PASP, 135, 038001
Bolan, P., Lemaux, B. C., Mason, C., et al. 2022, MNRAS, 517, 3263
Bouwens, R. J., Illingworth, G. D., Oesch, P. A., et al. 2015, ApJ, 803, 34
Bunker, A. J., Stanway, E. R., Ellis, R. S., & McMahon, R. G. 2004, MNRAS, 355, 374
Bunker, A. J., NIRSPEC Instrument Science Team, & JAESs Collaboration 2020, in Uncovering Early Galaxy Evolution in the ALMA and JWST Era, eds. E. da Cunha, J. Hodge, J. Afonso, L. Pentericci, & D. Sobral, 352, 342
Bunker, A. J., Cameron, A. J., Curtis-Lake, E., et al. 2023a, A&A, submitted [arXiv:2306.02467]
Bunker, A. J., Saxena, A., Cameron, A. J., et al. 2023b, A&A, 677, A88
Cai, Z., Fan, X., Yang, Y., et al. 2017, ApJ, 837, 71
Cain, C., D'Aloisio, A., Gangolli, N., & Becker, G. D. 2021, ApJ, 917, L37
Carniani, S., Venturi, G., Parlanti, E., et al. 2024, A&A, in press, https://doi.org/10.1051/0004-6361/202347230
Caruana, J., Bunker, A. J., Wilkins, S. M., et al. 2012, MNRAS, 427, 3055
Caruana, J., Bunker, A. J., Wilkins, S. M., et al. 2014, MNRAS, 443, 2831
Cassata, P., Tasca, L. A. M., Le Fèvre, O., et al. 2015, A&A, 573, A24
Christenson, H. M., Becker, G. D., Furlanetto, S. R., et al. 2021, ApJ, 923, 87
Cuby, J. G., Le Fèvre, O., McCracken, H., et al. 2003, A&A, 405, L19
Curtis-Lake, E., McLure, R. J., Pearce, H. J., et al. 2012, MNRAS, 422, 1425
Curtis-Lake, E., Carniani, S., Cameron, A., et al. 2023, Nat. Astron., 7, 622
de Graaff, A., Rix, H.-W., Carniani, S., et al. 2024, A&A, in press, https://doi.org/10.1051/0004-6361/202347755
Dey, A., Bian, C., Soifer, B. T., et al. 2005, ApJ, 629, 654
Dickinson, M., Giavalisco, M., & GOODS Team 2003, in The Mass of Galaxies at Low and High Redshift, eds. R. Bender, & A. Renzini, 324
Dijkstra, M., & Wyithe, J. S. B. 2010, MNRAS, 408, 352
Dijkstra, M., Mesinger, A., & Wyithe, J. S. B. 2011, MNRAS, 414, 2139
Drake, A. B., Neeleman, M., Venemans, B. P., et al. 2022, ApJ, 929, 86
Eisenstein, D. J., Willott, C., Alberts, S., et al. 2023, ApJS, submitted [arXiv:2306.02465]
Endsley, R., Stark, D. P., Chevallard, J., & Charlot, S. 2021, MNRAS, 500, 5229
Endsley, R., Stark, D. P., Bouwens, R. J., et al. 2022, MNRAS, 517, 5642
Erb, D. K., Steidel, C. C., Trainor, R. F., et al. 2014, ApJ, 795, 33
Fan, X., Strauss, M. A., Becker, R. H., et al. 2006, AJ, 132, 117
Fan, X., Bañados, E., & Simcoe, R. A. 2023, ARA&A, 61, 373
Ferruit, P., Jakobsen, P., Giardino, G., et al. 2022, A&A, 661, A81
Fontana, A., Vanzella, E., Pentericci, L., et al. 2010, ApJ, 725, L205
Fujimoto, S., Wang, B., Weaver, J., et al. 2023, ApJ, submitted [arXiv:2308.11609]
Fuller, S., Lemaux, B. C., Bradač, M., et al. 2020, ApJ, 896, 156
Furusawa, H., Kashikawa, N., Kobayashi, M. A. R., et al. 2016, ApJ, 822, 46
Gnedin, N. Y. 2000, ApJ, 535, 530
Guo, Y., Bacon, R., Wisotzki, L., et al. 2023, A&A, submitted [arXiv:2309.06311]
Harikane, Y., Ouchi, M., Ono, Y., et al. 2016, ApJ, 821, 123
Heintz, K. E., Watson, D., Brammer, G., et al. 2023, arXiv e-prints [arXiv:2306.00647]
Hoag, A., Bradač, M., Huang, K., et al. 2019, ApJ, 878, 12
Hutchison, T. A., Papovich, C., Finkelstein, S. L., et al. 2019, ApJ, 879, 70
Iye, M., Ota, K., Kashikawa, N., et al. 2006, Nature, 443, 186
Jakobsen, P., Ferruit, P., Alves de Oliveira, C., et al. 2022, A&A, 661, A80
Jung, I., Finkelstein, S. L., Larson, R. L., et al. 2022, ApJ, submitted [arXiv:2212.09850]
Jung, I., Finkelstein, S. L., Arrabal Haro, P., et al. 2023, ApJ, submitted [arXiv:2304.05385]
Kerutt, J., Wisotzki, L., Verhamme, A., et al. 2022, A&A, 659, A183
Kikuta, S., Matsuda, Y., Inoue, S., et al. 2023, ApJ, 947, 75
Larson, R. L., Finkelstein, S. L., Hutchison, T. A., et al. 2022, ApJ, 930, 104
Li, J., Emonts, B. H. C., Cai, Z., et al. 2021, ApJ, 922, L29
Marchi, F., Pentericci, L., Guaita, L., et al. 2019, A&A, 631, A19
Mason, C. A., & Gronke, M. 2020, MNRAS, 499, 1395
Mason, C. A., Treu, T., Dijkstra, M., et al. 2018, ApJ, 856, 2
Mason, C. A., Fontana, A., Treu, T., et al. 2019, MNRAS, 485, 3947
Matthee, J., Sobral, D., Boogaard, L. A., et al. 2019, ApJ, 881, 124
Matthee, J., Naidu, R. P., Pezzulli, G., et al. 2022, MNRAS, 512, 5960
Mesinger, A., & Furlanetto, S. 2007, ApJ, 669, 663
Mesinger, A., & Furlanetto, S. R. 2008, MNRAS, 385, 1348
Mesinger, A., Furlanetto, S., & Cen, R. 2011, MNRAS, 411, 955
Miralda-Escudé, J. 1998, ApJ, 501, 15
Morales, A. M., Mason, C. A., Bruton, S., et al. 2021, ApJ, 919, 120
Mortlock, D. 2016, Astrophys. Space Sci. Lib., 423, 187
Naidu, R. P., Tacchella, S., Mason, C. A., et al. 2020, ApJ, 892, 109
Newville, M., Stensitzki, T., Allen, D. B., et al. 2014, Astrophysics Source Code Library [record ascl:1606.014]
Oesch, P. A., van Dokkum, P. G., Illingworth, G. D., et al. 2015, ApJ, 804, L30
Oke, J. B., & Gunn, J. E. 1983, ApJ, 266, 713
Ono, Y., Ouchi, M., Mobasher, B., et al. 2012, ApJ, 744, 83
Pentericci, L., Vanzella, E., Fontana, A., et al. 2014, ApJ, 793, 113
Pentericci, L., Vanzella, E., Castellano, M., et al. 2018, A&A, 619, A147
Prieto-Lyon, G., Mason, C., Mascia, S., et al. 2023, ApJ, 956, 136
Reuland, M., van Breugel, W., Röttgering, H., et al. 2003, ApJ, 592, 755
Richard, J., Claeyssens, A., Lagattuta, D., et al. 2021, A&A, 646, A83
Rieke, M. J., Kelly, D. M., Misselt, K., et al. 2023, PASP, 135, 028001
Roberts-Borsani, G. W., Bouwens, R. J., Oesch, P. A., et al. 2016, ApJ, 823, 143
Roy, N., Henry, A., Treu, T., et al. 2023, ApJ, 952, L14
Saxena, A., Bunker, A. J., Jones, G. C., et al. 2024, A&A, in press, https://doi.org/10.1051/0004-6361/202347132
Schenker, M. A., Stark, D. P., Ellis, R. S., et al. 2012, ApJ, 744, 179
Schenker, M. A., Ellis, R. S., Konidaris, N. P., & Stark, D. P. 2014, ApJ, 795, 20
Shibuya, T., Ouchi, M., Harikane, Y., et al. 2018, PASJ, 70, S15
Song, M., Finkelstein, S. L., Livermore, R. C., et al. 2016, ApJ, 826, 113
Stark, D. P., Ellis, R. S., Chiu, K., Ouchi, M., & Bunker, A. 2010, MNRAS, 408, 1628
Stark, D. P., Ellis, R. S., & Ouchi, M. 2011, ApJ, 728, L2
Stark, D. P., Ellis, R. S., Charlot, S., et al. 2017, MNRAS, 464, 469
Steidel, C. C., Adelberger, K. L., Shapley, A. E., et al. 2000, ApJ, 532, 170
Tang, M., Stark, D. P., Chen, Z., et al. 2023, MNRAS, 526, 1657
Taylor, J., & Lidz, A. 2014, MNRAS, 437, 2542
Thai, T. T., Tuan-Anh, P., Pello, R., et al. 2023, A&A, 678, A139
Tilvi, V., Malhotra, S., Rhoads, J. E., et al. 2020, ApJ, 891, L10
Umeda, H., Ouchi, M., Nakajima, K., et al. 2023, arXiv e-prints [arXiv:2306.00487]
Vanzella, E., Pentericci, L., Fontana, A., et al. 2011, ApJ, 730, L35
Villanueva-Domingo, P., Gariazzo, S., Gnedin, N. Y., & Mena, O. 2018, JCAP, 2018, 024
Witstok, J., Smit, R., Saxena, A., et al. 2024, A&A, 682, A40
Yoshioka, T., Kashikawa, N., Inoue, A. K., et al. 2022, ApJ, 927, 32
Zahn, O., Mesinger, A., McQuinn, M., et al. 2011, MNRAS, 414, 727
Zhang, H., Cai, Z., Liang, Y., et al. 2024, ApJ, 961, 63
Zhu, Y., Becker, G. D., Bosman, S. E. I., et al. 2022, ApJ, 932, 76
Zitrin, A., Labbé, I., Belli, S., et al. 2015, ApJ, 810, L12

[1] Department of Physics, University of Oxford, Denys Wilkinson Building, Keble Road, Oxford OX1 3RH, UK
e-mail: gareth.jones@physics.ox.ac.uk
[2] Department of Physics and Astronomy, University College London, Gower Street, London WC1E 6BT, UK
[3] Kavli Institute for Cosmology, University of Cambridge, Madingley Road, Cambridge CB3 0HA, UK
[4] Cavendish Laboratory, University of Cambridge, 19 JJ Thomson Avenue, Cambridge CB3 0HE, UK
[5] Steward Observatory, University of Arizona, 933 N. Cherry Ave., Tucson, AZ 85721, USA
[6] Centro de Astrobiología (CAB), CSIC–INTA, Cra. de Ajalvir Km. 4, 28850 Torrejón de Ardoz, Madrid, Spain
[7] European Space Agency (ESA), European Space Astronomy Centre (ESAC), Camino Bajo del Castillo s/n, 28692 Villanueva de la Cañada, Madrid, Spain
[8] European Space Agency, ESA/ESTEC, Keplerlaan 1, 2201 AZ Noordwijk, The Netherlands
[9] Jodrell Bank Centre for Astrophysics, Department of Physics and Astronomy, School of Natural Sciences, The University of Manchester, Manchester M13 9PL, UK
[10] School of Physics, University of Melbourne, Parkville 3010, VIC, Australia
[11] ARC Centre of Excellence for All Sky Astrophysics in 3 Dimensions (ASTRO 3D), Stromlo, ACT 2611, Australia
[12] Scuola Normale Superiore, Piazza dei Cavalieri 7, 56126 Pisa, Italy

[13] Sorbonne Université, CNRS, UMR 7095, Institut d'Astrophysique de Paris, 98 bis bd Arago, 75014 Paris, France
[14] European Southern Observatory, Karl-Schwarzschild-Strasse 2, 85748 Garching, Germany
[15] Centre for Astrophysics Research, Department of Physics, Astronomy and Mathematics, University of Hertfordshire, Hatfield AL10 9AB, UK
[16] Center for Astrophysics | Harvard & Smithsonian, 60 Garden St., Cambridge, MA 02138, USA
[17] Department of Physics and Astronomy, The Johns Hopkins University, 3400 N. Charles St., Baltimore, MD 21218, USA
[18] AURA for European Space Agency, Space Telescope Science Institute, 3700 San Martin Drive, Baltimore, MD 21210, USA
[19] Department of Astronomy, University of Wisconsin-Madison, 475 N. Charter St., Madison, WI 53706, USA
[20] Max-Planck-Institut für Astronomie, Königstuhl 17, 69117 Heidelberg, Germany
[21] Department of Astronomy and Astrophysics, University of California, Santa Cruz, 1156 High Street, Santa Cruz, CA 95064, USA
[22] Astrophysics Research Institute, Liverpool John Moores University, 146 Brownlow Hill, Liverpool L3 5RF, UK
[23] NSF's National Optical-Infrared Astronomy Research Laboratory, 950 North Cherry Avenue, Tucson, AZ 85719, USA
[24] NRC Herzberg, 5071 West Saanich Rd, Victoria, BC V9E 2E7, Canada

Appendix A: Additional figure

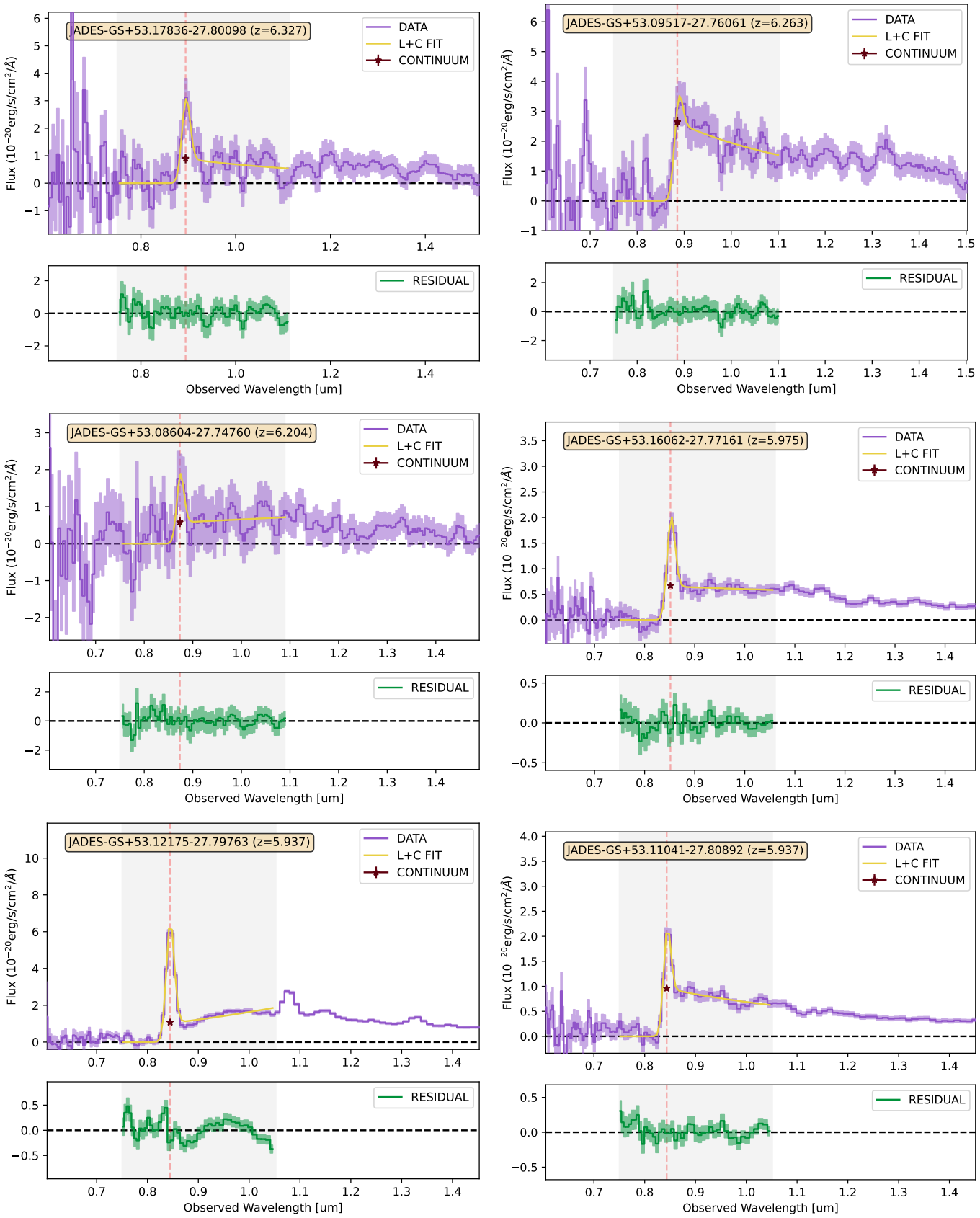

Fig. A.1. See the caption of Figure 2.

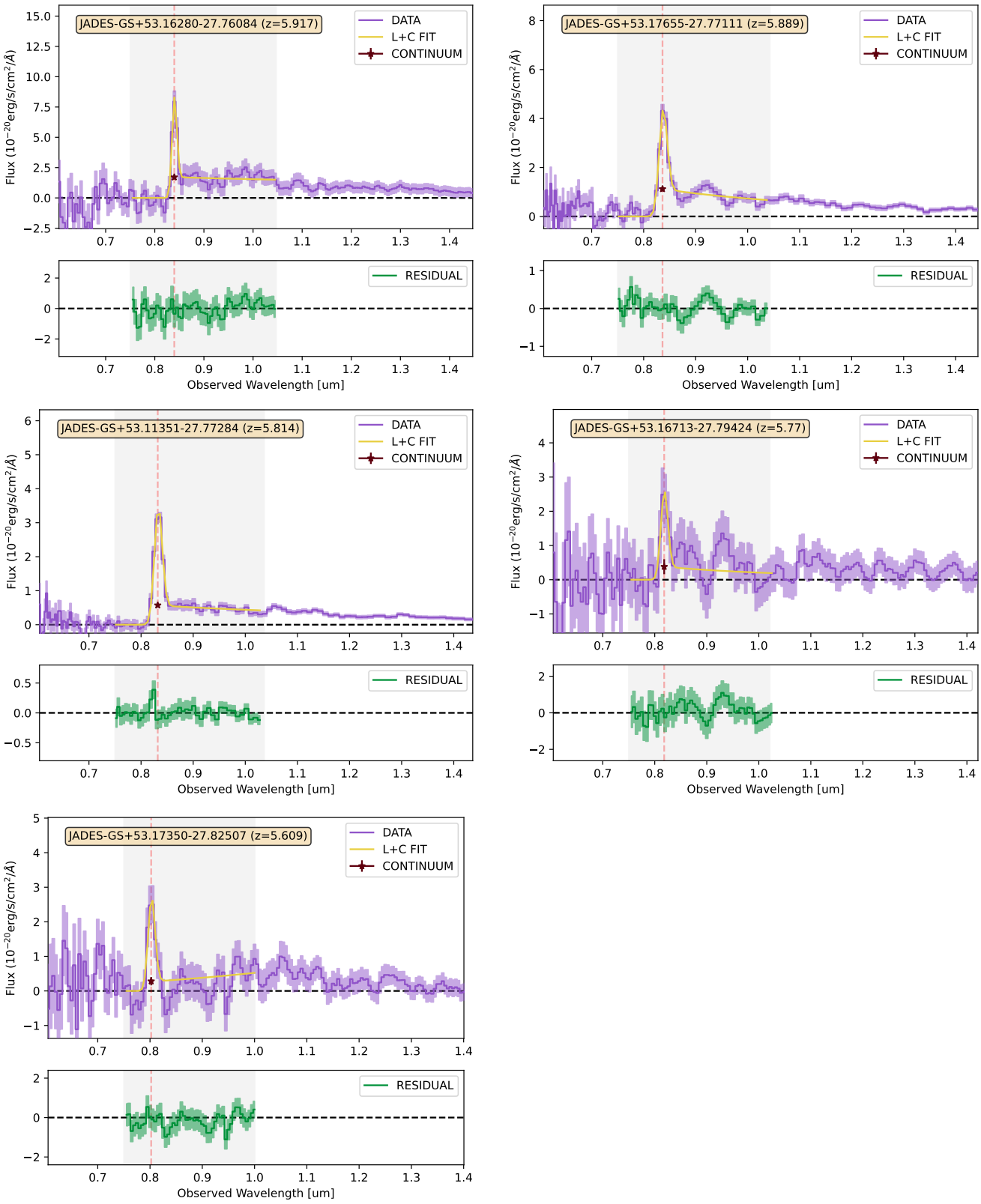

Fig. A.1. continued.

Appendix B: Damping wing in R100

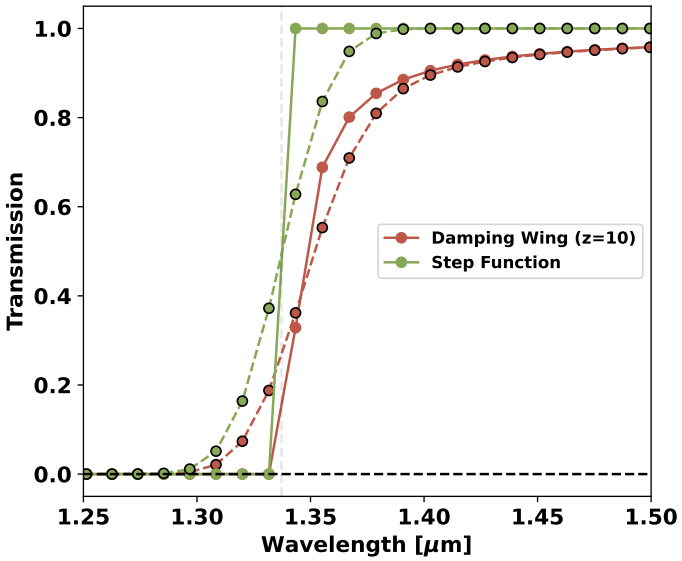

Fig. B.1. Transmission models of a damping wing (brown lines) and a step function (green lines) for a $z = 10$ source. We include the intrinsic model, re-gridded to match our R100 observations (solid lines), and the dispersed version of this model (dashed lines). The Lyα wavelength is shown by a faint vertical line.

In this work we assumed that the Lyman break can be approximated by a step function. To test whether this is appropriate for our R100 spectra, we considered the wavelength-dependent damping wing optical depth formalism of Miralda-Escudé (1998) for a source at redshift z_s:

$$\tau(\Delta\lambda) = \frac{\tau_o R_\alpha}{\pi}(1+\delta)^{3/2}\left[F(x_2) - F(x_1)\right], \quad \text{(B.1)}$$

where $\Delta\lambda$ is the wavelength offset from the redshifted centroid of Lyα (λ_α), $\delta \equiv \Delta\lambda/[\lambda_\alpha(1+z_s)]$, and we assumed $\tau_o = \tau_{GP} = (7.16\times10^5)\times\left(\frac{1+z_s}{10}\right)^{3/2}$ and $R_\alpha = 2.0136\times10^{-8}$ from Mesinger & Furlanetto (2008). F(x) is given as

$$F(x) = \frac{x^{9/2}}{1-x} + \frac{9x^{7/2}}{7} + \frac{9x^{5/2}}{5} + 3x^{3/2} + 9x^{1/2} - \frac{9}{2}\log\frac{1+x^{1/2}}{1-x^{1/2}}, \quad \text{(B.2)}$$

with $x_1 = (1+z_n)/[(1+z_s)(1+\delta)]$ and $x_2 = 1/(1+\delta)$ where z_n is the redshift where absorption by the IGM is assumed to be negligible (we used the standard assumption of $z_n = 6$; e.g. Mortlock 2016; Fan et al. 2023). We note that in this form, the model assumes a uniform X_{HI} between $z_n < z < z_s$ (here assumed to be unity) and a no IGM absorption below $z < z_n$.

As z_s approaches z_n from high values, the damping wing begins to approximate a step function. For sources below z_n (which includes most sources in our sample), the IGM is expected to have little effect, and a step function is thus appropriate. But for sources above z_n, it is possible that the damping wing will have an effect.

To investigate this, the optical depth model is used to create a transmission spectrum for a source at $z_s = 10$, using the same wavelength grid as our R100 spectra (see the solid lines in Figure B.1). To account for the instrumental dispersion, this model is convolved with a Gaussian with $\sigma = \sigma_R$ (see Section 3.1 and the dashed lines in Figure B.1).

For $\lambda \gg \lambda_{Ly\alpha}$ or $\lambda \ll \lambda_{Ly\alpha}$, the two convolved curves are similar (i.e. either 0 or unity). But in this case of a $z = 10$ source, the curves differ at $\lambda \sim \lambda_{Ly\alpha}$, with a discrepancy of up to $\sim 20\%$. This strong difference can be detected for some sources, and will be used in future works to place constraints on the proximity zones and IGM neutral fraction of $z > 8$ sources in JADES (e.g. Jakobsen et al., in prep.). Indeed, multiple studies have now used JWST/NIRSpec observations to constrain the Lyα damping wing (e.g. Fujimoto et al. 2023; Heintz et al. 2023; Umeda et al. 2023).

Throughout this work, we assume that the transmission function for galaxies in our sample is a simple step function (i.e. 100% transmission redwards of $\lambda_{Ly\alpha}$). In reality, damping wings will affect all of the $z \gtrsim 8$ sources, resulting in low transmission at $\lambda_{Ly\alpha}$ and thus making it more difficult to detect Lyα emission. For the six $z > 8$ sources in our sample (none of which are detected in Lyα emission), we note that this is not accounted for in our $\mathrm{REW}_{Ly\alpha}$ upper limits, so these may be slightly underestimated. But a full treatment of the damping wing effect is beyond the scope of this paper and will be fully explored in a future analysis.

Appendix C: Table of best-fit parameters

Table C.1. Results of fitting the R100 spectra of each galaxy.

ID *JADES-GS*	z_{sys}	Tier	M_{UV}	$S_C(\lambda_{Ly\alpha,obs})$ 10^{-21} erg s^{-1} cm^{-2} Å^{-1}	$F_{Ly\alpha,R100}$ 10^{-19} erg s^{-1} cm^{-2}	$REW_{Ly\alpha,R100}$ Å	$F_{Ly\alpha,R100}$ 10^{-19} erg s^{-1} cm^{-2}	$REW_{Ly\alpha,R100}$ Å
+53.15682-27.76716	7.982	Deep/HST	-18.71 ± 0.05	2.9 ± 0.1	7 ± 1	27 ± 5	7 ± 1	27 ± 8
+53.13347-27.76037	7.660	Medium/HST	-20.43 ± 0.03	21.9 ± 0.6	25 ± 4	13 ± 2	42 ± 3	22 ± 3
+53.16746-27.77201	7.276	Deep/HST	-17.00 ± 0.25	1.3 ± 0.4	15 ± 7	134 ± 50	23 ± 2	207 ± 27
+53.15579-27.81520	6.718	Deep/HST	-18.51 ± 0.08	2.9 ± 0.4	17 ± 5	77 ± 22	27 ± 3	122 ± 27
+53.16904-27.77884	6.633	Deep/HST	-18.76 ± 0.04	6.4 ± 0.3	21 ± 3	44 ± 6	22 ± 5	45 ± 20
+53.13492-27.77271	6.336	Deep/HST	-20.11 ± 0.01	25.3 ± 0.8	72 ± 6	39 ± 3	77 ± 4	41 ± 4
+53.17836-27.80098	6.327	Medium/HST	-18.75 ± 0.18	9.0 ± 1.8	57 ± 20	86 ± 26	43 ± 12	65 ± 36
+53.09517-27.76061	6.263	Medium/HST	-19.85 ± 0.06	26.4 ± 1.7	42 ± 9	22 ± 5	31 ± 8	16 ± 8
+53.08604-27.74760	6.204	Medium/HST	-18.93 ± 0.14	5.8 ± 1.3	29 ± 13	70 ± 27	48 ± 21	114 ± 99
+53.16062-27.77161	5.975	Deep/HST	-18.63 ± 0.04	6.7 ± 0.3	33 ± 3	72 ± 6	22 ± 5	47 ± 20
+53.12175-27.79763	5.937	Deep/HST	-19.83 ± 0.01	10.7 ± 0.7	123 ± 13	165 ± 15	106 ± 9	142 ± 25
+53.11041-27.80892	5.937	Deep/HST	-18.68 ± 0.03	9.6 ± 0.5	29 ± 3	44 ± 5	29 ± 6	43 ± 19
+53.16280-27.76084	5.917	Medium/HST	-19.60 ± 0.08	17.1 ± 1.8	90 ± 17	76 ± 12	112 ± 19	95 ± 32
+53.17655-27.77111	5.889	Deep/HST	-18.72 ± 0.06	11.2 ± 1.1	74 ± 12	95 ± 12	–	–
+53.11351-27.77284	5.814	Deep/HST	-18.18 ± 0.05	5.7 ± 0.5	60 ± 8	153 ± 17	38 ± 5	97 ± 25
+53.16713-27.79424	5.770	Medium/HST	-17.32 ± 0.60	3.8 ± 2.2	41 ± 36	159 ± 106	–	–
+53.17350-27.82507	5.609	Medium/JWST	-18.23 ± 0.19	2.8 ± 1.2	44 ± 29	238 ± 120	–	–
+53.16477-27.77463	11.900	Deep/HST	-19.36 ± 0.05	1.6 ± 0.2	< 5	< 23	–	–
+53.15884-27.77349	9.870	Deep/HST	-18.45 ± 0.11	1.1 ± 0.2	< 7	< 58	–	–
+53.16735-27.80750	9.690	Deep/HST	-19.27 ± 0.04	3.1 ± 0.1	< 5	< 14	–	–
+53.11243-27.77461	9.440	Deep/HST	-20.36 ± 0.01	8.8 ± 0.2	< 5	< 5	–	–
+53.16446-27.80218	8.482	Deep/HST	-17.54 ± 0.20	0.5 ± 0.1	< 8	< 161	–	–
+53.08722-27.77706	7.580	Medium/HST	-19.03 ± 0.20	6.8 ± 1.1	< 56	< 95	–	–
+53.18343-27.79097	7.429	Medium/JWST	-20.00 ± 0.05	11.3 ± 0.7	< 37	< 39	–	–
+53.19105-27.79731	7.266	Medium/JWST	-19.15 ± 0.10	6.0 ± 0.5	< 30	< 60	–	–
+53.18714-27.80129	7.264	Medium/JWST	-18.41 ± 0.20	3.5 ± 0.6	< 35	< 122	–	–
+53.15283-27.80194	7.262	Deep/HST	-17.95 ± 0.10	2.0 ± 0.3	< 8	< 48	–	–
+53.18374-27.79390	7.262	Medium/JWST	-17.94 ± 0.36	2.9 ± 0.8	< 40	< 170	–	–
+53.16483-27.78826	7.250	Medium/HST	-19.08 ± 0.18	8.9 ± 1.2	< 58	< 79	–	–
+53.16172-27.78539	7.240	Medium/HST	-19.47 ± 0.18	7.7 ± 1.0	< 65	< 103	–	–
+53.16556-27.77266	7.240	Medium/HST	-18.32 ± 0.29	4.6 ± 1.8	< 45	< 119	–	–
+53.11833-27.76901	7.206	Deep/HST	-18.80 ± 0.05	5.1 ± 0.3	< 10	< 25	–	–
+53.13806-27.78186	7.140	Medium/HST	-18.66 ± 0.22	1.8 ± 0.4	< 46	< 312	–	–
+53.13423-27.76891	7.052	Deep/HST	-18.84 ± 0.06	7.6 ± 0.5	< 12	< 19	–	–
+53.17688-27.78156	7.002	Medium/JWST	-17.94 ± 0.28	1.2 ± 0.5	< 31	< 334	–	–
+53.18302-27.78946	6.951	Medium/JWST	-17.92 ± 0.27	1.4 ± 0.5	< 30	< 271	–	–

Notes. We include the best-fit M_{UV} (from the spectrum; see Appendix D) and continuum flux at the redshifted Lyα wavelength. Line fluxes and REWs from the R100 data alone are shown first. Next, REW values derived by combining the R1000-based Lyα fluxes from Saxena et al. (2024) with our R100 continuum values are presented for reference. Systemic redshifts (based on fits to strong optical lines) have uncertainty of 0.001 (Bunker et al. 2023a). Upper limits are given as 3σ. Galaxies detected in Lyα emission in the R100 data are listed first.

Table C.1. continued.

ID *JADES-GS*	z_{sys}	Tier	M_{UV}	$S_C(\lambda_{Ly\alpha,obs})$ 10^{-21} erg s^{-1} cm^{-2} Å^{-1}	$F_{Ly\alpha,R100}$ 10^{-19} erg s^{-1} cm^{-2}	$REW_{Ly\alpha,R100}$ Å	$F_{Ly\alpha,R100}$ 10^{-19} erg s^{-1} cm^{-2}	$REW_{Ly\alpha,R100}$ Å
+53.11730-27.76408	6.930	Deep/HST	−18.69 ± 0.07	4.7 ± 0.3	< 13	< 35	–	–
+53.14771-27.71537	6.846	Medium/HST	−20.33 ± 0.05	22.3 ± 1.3	< 45	< 26	–	–
+53.11817-27.79302	6.800	Medium/HST	−19.01 ± 0.13	7.2 ± 1.1	< 41	< 74	–	–
+53.11634-27.76194	6.794	Medium/HST	−18.88 ± 0.12	7.3 ± 1.1	< 34	< 61	–	–
+53.15138-27.81917	6.711	Deep/HST	−17.96 ± 0.07	3.8 ± 0.3	< 7	< 25	–	–
+53.10538-27.72347	6.636	Medium/HST	−20.48 ± 0.04	27.0 ± 1.4	< 63	< 31	–	–
+53.15160-27.78791	6.629	Medium/JWST	−17.02 ± 0.34	1.2 ± 0.5	< 20	< 208	–	–
+53.16288-27.76928	6.624	Deep/HST	−17.61 ± 0.20	2.0 ± 0.5	< 16	< 107	–	–
+53.13743-27.76519	6.622	Medium/HST	−18.43 ± 0.26	6.8 ± 2.0	< 51	< 97	25 ± 10	48 ± 40
+53.16951-27.75331	6.620	Medium/HST	−19.34 ± 0.11	12.9 ± 1.6	< 46	< 47	–	–
+53.12731-27.78805	6.390	Medium/HST	−19.43 ± 0.13	18.4 ± 2.1	< 62	< 46	–	–
+53.12556-27.78676	6.390	Medium/HST	−18.36 ± 0.34	5.7 ± 2.0	< 59	< 139	–	–
+53.19660-27.81345	6.340	Medium/HST	−18.24 ± 0.28	5.4 ± 1.0	< 42	< 105	–	–
+53.17582-27.77446	6.336	Deep/HST	−18.74 ± 0.06	6.4 ± 0.6	< 15	< 32	–	–
+53.16660-27.77240	6.330	Deep/HST	−18.56 ± 0.05	6.7 ± 0.4	< 9	< 18	–	–
+53.15516-27.76072	6.314	Medium/HST	−19.42 ± 0.05	15.9 ± 0.8	< 27	< 23	–	–
+53.16613-27.77204	6.300	Medium/HST	−18.47 ± 0.25	7.3 ± 1.9	< 52	< 98	–	–
+53.16238-27.80332	6.298	Deep/HST	−16.33 ± 0.62	1.0 ± 0.6	< 15	< 195	–	–
+53.08311-27.78635	6.260	Medium/HST	−19.72 ± 0.09	17.8 ± 2.2	< 62	< 48	–	–
+53.16902-27.80079	6.250	Medium/HST	−18.95 ± 0.16	10.9 ± 1.5	< 48	< 61	–	–
+53.20800-27.79005	6.180	Medium/HST	−19.25 ± 0.16	5.2 ± 1.8	< 90	< 242	–	–
+53.15613-27.77584	6.107	Deep/HST	−19.02 ± 0.04	8.4 ± 0.6	< 11	< 19	–	–
+53.15953-27.77152	6.100	Medium/HST	−20.43 ± 0.04	40.7 ± 1.7	< 43	< 15	–	–
+53.19588-27.76843	6.060	Medium/HST	−18.80 ± 0.16	7.7 ± 1.6	< 41	< 75	–	–
+53.17324-27.79567	6.000	Medium/HST	−19.66 ± 0.06	15.3 ± 1.1	< 33	< 31	–	–
+53.17264-27.76706	5.990	Medium/HST	−19.02 ± 0.12	9.5 ± 1.4	< 42	< 63	–	–
+53.19938-27.79627	5.980	Medium/HST	−19.44 ± 0.09	17.2 ± 1.4	< 42	< 35	–	–
+53.14902-27.78070	5.956	Medium/JWST	−17.85 ± 0.34	4.4 ± 1.6	< 37	< 121	–	–
+53.11911-27.76080	5.949	Deep/HST	−19.42 ± 0.02	17.7 ± 0.5	< 7	< 6	–	–
+53.11264-27.77262	5.934	Medium/HST	−18.41 ± 0.22	4.9 ± 1.7	< 41	< 120	–	–
+53.12654-27.81809	5.932	Deep/HST	−18.93 ± 0.04	10.7 ± 0.6	< 10	< 13	–	–
+53.13044-27.80236	5.930	Medium/HST	−19.17 ± 0.11	7.8 ± 1.8	< 71	< 131	–	–
+53.15218-27.77840	5.927	Medium/JWST	−16.99 ± 0.43	0.9 ± 0.5	< 19	< 316	–	–
+53.10547-27.76115	5.925	Medium/HST	−20.09 ± 0.05	18.0 ± 1.4	< 42	< 33	–	–
+53.12259-27.76057	5.920	Deep/HST	−19.64 ± 0.02	24.0 ± 0.6	< 9	< 6	–	–
+53.14987-27.75283	5.919	Medium/HST	−19.39 ± 0.07	13.7 ± 1.0	< 33	< 35	–	–
+53.17752-27.80252	5.860	Medium/HST	−19.15 ± 0.11	15.2 ± 1.3	< 40	< 38	–	–
+53.14197-27.75523	5.827	Medium/HST	−19.70 ± 0.08	24.8 ± 1.6	< 41	< 24	–	–
+53.16730-27.80287	5.818	Deep/HST	−17.89 ± 0.09	3.2 ± 0.3	< 9	< 43	–	–
+53.15407-27.76607	5.807	Deep/HST	−18.94 ± 0.04	10.3 ± 0.6	< 9	< 13	–	–
+53.12554-27.75505	5.780	Medium/HST	−19.35 ± 0.11	9.3 ± 1.7	< 57	< 90	–	–
+53.13385-27.77858	5.778	Medium/JWST	−16.72 ± 0.73	2.1 ± 1.3	< 28	< 200	–	–
+53.14505-27.81643	5.774	Deep/HST	−18.05 ± 0.10	4.7 ± 0.7	< 13	< 40	–	–
+53.11537-27.81477	5.770	Deep/HST	−19.32 ± 0.03	14.4 ± 0.7	< 12	< 13	–	–
+53.11775-27.81653	5.761	Medium/JWST	−17.84 ± 0.32	6.2 ± 1.7	< 36	< 85	–	–
+53.21160-27.79639	5.760	Medium/HST	−19.35 ± 0.10	7.3 ± 1.1	< 43	< 88	–	–
+53.13059-27.80771	5.617	Deep/HST	−18.58 ± 0.09	9.9 ± 1.3	< 18	< 27	–	–
+53.18064-27.82239	5.606	Medium/JWST	−20.12 ± 0.03	29.3 ± 1.4	< 29	< 15	–	–

Appendix D: M_{UV} derivation

Due to the high quality of the NIRSpec spectra, we are able to derive $M_{1500\,Å}$ absolute magnitudes (M_{UV}) directly from the observed data. First, the observed data are shifted from the observed to rest frame by multiplying all flux values (i.e. f_λ) by $1+z$ and dividing all wavelength values by the same factor. The rest-frame f_λ values are converted to a f_ν:

$$f_\nu = f_\lambda \lambda^2 / c, \tag{D.1}$$

where c is the speed of light. We collected and averaged all f_ν values that lie between 1400 and 1600 Å (rest-frame) and used this average value ($\bar{f}_\nu$) to derive an apparent AB magnitude (Oke & Gunn 1983):

$$m_{1500} = -2.5 \log_{10}(\bar{f}_\nu) - 48.60, \tag{D.2}$$

which we converted to an absolute magnitude via

$$M_{\rm UV} = m_{1500} - 5 \log_{10}(D_L[Mpc]) - 25. \tag{D.3}$$

An error was estimated by calculating the root mean square noise level of the f_ν values between 1400−1600 Å from the error spectrum and perturbing $\bar{f}_\nu$ by this value.

Appendix E: Comparison data

As one of the brightest emission lines for star-forming galaxies at high-redshift, Lyα has been studied in numerous galaxies over the past decades. While the subset of JADES that we analyse in this work offers the opportunity to explore the Lyα properties of galaxies between $z \sim 5-11$, our conclusions are strengthened by the addition of archival data. Here, we collected a large literature sample of galaxies with reported spatial positions, spectroscopic redshifts, Lyα equivalent widths from spectral observations, and M_{UV} values. Unless otherwise stated, $z_{sys} = z_{Ly\alpha}$ and $M_{UV} = M_{1500}$. The details of our comparison sample are given below[3]. To avoid repeated galaxies, we searched for entries within 0.25″ of each other and excluded the older measurement.

Followup spectroscopy of bright LAEs discovered in the Systematic Identification of LAEs for Visible Exploration and Reionization Research Using Subaru HSC (SILVERRUSH) with a variety of ground-based telescopes resulted in numerous detections (Shibuya et al. 2018). The continuum level underlying Lyα was found by extrapolating from red filters ($\beta = -2$), while M_{UV} was estimated from the observed spectra.

We also included the large survey CANDELSz7 (Pentericci et al. 2018), a large programme that observed star-forming galaxies at $z \sim 6$ and $z \sim 7$ in the GOODS-S, United Kingdom Infrared Telescope (UKIRT) Infrared Deep Sky Survey (UKIDSS) Ultra-Deep Survey (UDS), and Cosmic Evolution Survey (COSMOS) fields with the FOcal Reducer/low dispersion Spectrograph 2 (FORS2) on the Very Large Telescope (VLT). We included all galaxies with good quality flags (i.e. A, A/B, and B) and Lyα flux estimates. M_{UV} values were estimated using fits to photometry from the Cosmic Assembly Near-infrared Deep Extragalactic Legacy Survey (CANDELS), while the REW was derived by fitting the observed spectra. Six sources were also observed with the VLT Multi Unit Spectroscopic Explorer (MUSE) by Kerutt et al. (2022), so they are not included.

Next, we included the results of studies that used Keck/MOSFIRE. Jung et al. (2022) observed eight $z \sim 7-8$ galaxies in CANDELS Extended Groth Strip (EGS) and used an asymmetric Gaussian to fit the Lyα emission. We excluded one source that lacks a spectroscopic redshift and a number of galaxies with only upper limits on $REW_{Ly\alpha}$. Four galaxies in this sample were likely re-observed in Tang et al. (2023), so they were also excluded. While Tilvi et al. (2020) observed three galaxies in group at $z = 7.7$, we took the one source with M_{UV} calculated by Tang et al. (2023), or $z8\_5$ (EGS-zs8-1 in Oesch et al. 2015). Song et al. (2016) detected one galaxy in Lyα emission ($z7\_GSD\_3811$), whose emission was fit with an asymmetric profile. Hoag et al. (2019) detected Lyα emission from two galaxies that are strongly lensed by galaxy clusters. Values are magnification-corrected, and equivalent width is calculated by dividing the line flux by HST WFC3/F160W continuum flux.

Keck DEep Imaging Multi-Object Spectrograph (DEIMOS) observations by Ono et al. (2012) resulted in line detections for three $z \sim 7$ galaxies in the Subaru Deep Field (SDF) and GOODS-N. The continuum properties were derived from a fit to the photometry. Further Keck/DEIMOS observations revealed 36 LAEs (Fuller et al. 2020). We note that SDF-63544 is also known as IOK-1 (e.g. Iye et al. 2006). Additional Keck observations resulted in three detections of Lyα with the Low Resolution Imaging Spectrometer (LRIS) and NIRSPEC spectrograph (Schenker et al. 2012), where the continuum was estimated by extrapolating a power-law model ($\beta = -2$) from a red filter.

Two works used the VLT/FORS2 spectrograph (Cuby et al. 2003; Vanzella et al. 2011). For these, we took M_{UV} from the compilation of Matthee et al. (2019). Additionally, the Gemini Multi-Object Spectrograph (GMOS) on the 8.2m Gemini Telescopes were used to observe one target. The resulting spectra were fit with templates, resulting in a Lyα REW and M_{1350}.

The Binospec spectrograph on the 6.5 m MMT telescope was used to observe eight UV-bright ($M_{UV} \sim -22$) galaxies at $z \sim 7$ selected from the Atacama Large Millimeter/submillimeter Array (ALMA) Reionization-Era Bright Emission Line Survey (REBELS; Endsley et al. 2022). Red bands were used to estimate the Lyα continuum, while $M_{UV} \equiv M_{1600}$.

VLT/MUSE features a bluer spectral range (0.465 − 0.930 μm[4]) with respect to the JWST/NIRSpec PRISM/CLEAR filter–disperser combination (0.6 − 5.3 μm), allowing it to probe Lyα to lower redshifts ($z \sim 2.8-6.7$). Through the MUSE-WIDE and MUSE-DEEP surveys, Kerutt et al. (2022) present the Lyα equivalent widths for 1920 galaxies over the full redshift range accessible to MUSE. The continuum level at $\lambda_{Ly\alpha}$ is estimated from photometry, while Lyα is measured from each MUSE data cube.

We also included ten galaxies in the Abell 2744 cluster from the recent work of Prieto-Lyon et al. (2023), who analysed data from the GLASS-JWST Early Release Science programme. M_{UV} values were derived from spectral energy distribution fits to HST and JWST photometry, while $REW_{Ly\alpha}$ is taken from the MUSE observations of Richard et al. (2021). The systemic redshift is derived from fits to optical lines as observed by JWST.

Finally, we included results from the recent work of Tang et al. (2023), who used the MSA of JWST/NIRSpec (R100 and R1000) to extract spectra and continuum estimates for ten sources. Four sources feature small spatial offsets (< 0.1″) and redshift differences ($\delta z \sim 0.25 - 0.35$) with sources observed with Keck/MOSFIRE by Tang et al. (2023). Since the red-

[3] A full machine readable table of the comparison sample is available in electronic form at the CDS.

[4] https://www.eso.org/sci/facilities/paranal/instruments/muse/inst.html

shift difference may be explained by a difference in methods (i.e. photometric versus spectroscopic), we assumed that these are the same galaxies. Here, $z_{sys} = z_{[OIII]5007}$. Lyα and continuum properties were extracted from the CEERS spectra and from photometry, respectively. The NIRSpec-based Lyα properties agree with ground-based REW measurements, suggesting the absence of calibration issues. A few of these sources were known by other names in previous studies: CEERS-1019 is EGSY8p7 (Zitrin et al. 2015), CEERS-1029 is EGS_z910_44164 (Larson et al. 2022), and CEERS-698 is EGS-zs8-2 (Roberts-Borsani et al. 2016).

Appendix F: REW-M_{UV} simulation

In Section 4.2, we found that the $REW_{Ly\alpha}$ and M_{UV} of our sample showed an apparent positive relation, such that more UV-faint galaxies featured larger Lyα equivalent widths. But since REW is a ratio of line flux to continuum flux, it is possible that this relation is influenced by the sensitivity limit of our sample and fitting method (i.e. we may miss Lyα-faint galaxies). In this section, we test this possibility using a method similar to our completeness analysis (Section 3.5).

For each survey tier (Deep/HST, Medium/HST, and Medium/JWST), we created 750 model spectra by sampling uniformly for several properties ($5.6 < z < 12.0$, $-20.4 < M_{UV} < -16.4$, spectral slope $-2 < n < 2$, $0.1 < F_R < 0.8$) and log-uniformly for Lyα equivalent width ($1 < REW_{Ly\alpha} < 750$ Å). Gaussian noise was added to each model spectrum based on the corresponding mean error spectrum, and the resulting spectrum was fit with our routine.

In Figure F.1, we show the intrinsic distribution of REW versus M_{UV} in blue, and display the resulting best-fit values as red-outlined black circles. Upper limits on REW (3σ) are shown as downward arrows. It is clear that we do not capture the full distribution, as galaxies in the lower-right corner (UV-faint and low-REW) are not able to be fit. From this test, it is clear that our sample and fitting approach may result in a false positive trend of REW with M_{UV}, due to sensitivity limits.

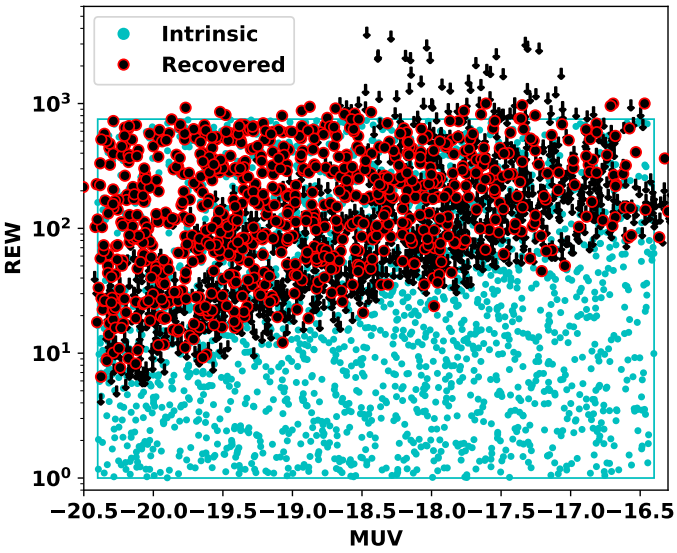

Fig. F.1. Results of fitting a sample of simulated galaxies. The intrinsic distribution of REW and M_{UV} for the simulated galaxies are shown as cyan circles, with a cyan rectangle outlining the region. The best-fit values and 3σ upper limits are shown as red-outlined circles and black arrows, respectively.